THE ASTROPHYSICAL JOURNAL, 370:643–669, 1991 April 1

A RELATIVISTIC MODEL OF PULSAR POLARIZATION

M. BLASKIEWICZ[1]
Department of Physics and National Astronomy and Ionosphere Center, Cornell University
J. M. CORDES[1]
Astronomy Department and National Astronomy and Ionosphere Center, Cornell University
AND
I. WASSERMAN[1]
Astronomy Department, Cornell University
Received 1990 July 12; accepted 1990 September 11

ABSTRACT

A relativistic model of pulsar polarization is presented which involves radio emission from the open field line region at radii well within the light cylinder. The model incorporates relativistic plasma flow when the corotation component of the plasma velocity is included. The model predicts that the centroid of the position angle curve arrives later than the centroid of the intensity profile by an amount $4r/c$, where r is the emission radius. Our assumptions should hold for coherent curvature emission and for plasma maser emission mechanisms that do not employ a cyclotron resonance, as long as propagation effects are not too large. Application to pulsars with well-ordered position angle swings and periods between 0.06 and 3.7 s gives emission radii of not more than 2000 km for 0.43 and 1.4 GHz. In most cases, the upper bound is 100–300 km, and in 11 cases the emission radii are known within error bars of less than 50%. The results agree well with the emission radii predicted using a radius–to–pulse-width mapping. We find that the symmetry breaking effects of the corotation velocity may help explain a general asymmetry found in pulsar intensity profiles and may strongly affect the intensity profiles of short-period pulsars.

Subject headings: polarization — pulsars — relativity

1. INTRODUCTION

For two decades the rotating vector model (RVM) of Radhakrishnan and Cooke (1969) has been the standard model used to interpret pulsar polarization. The RVM assumes a strong dipolar magnetic field that collimates a relativistic flow of plasma. Radio emission is amplified by an instability but is assumed to have polarization properties similar to those of incoherent radiation. The emitted radiation is then polarized along, or orthogonal to, the curvature of the magnetic field.

The RVM has been used to show that the dominant magnetic field in the emission region is often consistent with being dipolar and to study the shape of pulsar radio beams (Narayan & Vivekanand 1983, hereafter NV83; Lyne & Manchester 1988, hereafter LM88). These studies show that the boundary of the emission region is often nearly symmetric with respect to the plane containing the spin and magnetic axes. It also appears that the emission region may have a nearly circular cross section (LM88), possibly with some meridional compression (Biggs 1990).

There have been some observationally motivated extensions of the RVM, most notably the recognition of "orthogonal" polarization modes (Manchester, Taylor, & Huguenin 1975; Backer, Rankin, & Campbell 1975; Cordes & Hankins 1977; Cordes, Rankin, & Backer 1978; Backer & Rankin 1980; Stinebring et al. 1984a, b; hereafter MTH75, BRC75, CH77, CRB78, BR80, and S84a, b, respectively). These orthogonal modes are inferred from nearly instantaneous changes in the polarization state of the radio emission and have been attributed to the superposition of two, nearly orthogonal polarization states.

[1] Postal address: Space Sciences Building, Cornell University, Ithaca, NY 14853.

Theoretical modifications of the RVM have been put forth by Ferguson (1973, 1976), who includes some relativistic effects but not of the type considered by us. Shitov (1985, hereafter S85) models corrections to the dipole field due to wave energy losses at the spin frequency. In Shitov's model, departures from RVM predictions are due to an asymmetry in the emission region caused by twisting of the magnetic field lines. Barnard (1986, hereafter B86) introduced a model of pulsar polarization which includes propagation effects. In Barnard's model, departures from RVM predictions depend on the plasma parameters and on the form of the magnetic field near the light cylinder.

In this paper we extend the RVM to include first-order, special relativistic effects: gravity is ignored. We assume that the large-scale magnetic field in the emission region is dipolar, with a force-free plasma in regions threaded by closed field lines (Goldreich & Julian 1969; Sturrock 1971; Ruderman & Sutherland 1975; Michel 1982; Beskin, Gurevich, & Istomin 1983; hereafter GJ69, S71, RS75, M82, and BGI83, respectively). Accelerating potentials and magnetospheric currents are assumed to be limited by the values appropriate to the homopolar generator model (GJ69; S71; RS75; M82; BGI83). With these assumptions the velocity of relativistic plasma in the emission region is obtained. We find that the plasma velocity is nearly along the magnetic field, so the salient features of the RVM are retained. In addition to the velocity along the field, there is another component, which is simply the local corotation velocity. For emission well within the light cylinder we argue that additional corrections to the plasma velocity, due to an accelerating potential and magnetospheric currents, are small in comparison with the corotation velocity. This paper is concerned with calculating the effects of the corotation velocity on pulsar radio emission and testing for the presence of those effects.

In § 2 we consider the ambient conditions well within the light cylinder. Assuming a very strong, dipolar magnetic field, the plasma velocity and acceleration are used to obtain the polarization and emission direction of the radiation. For emission at a single radius, analytic formulae for the polarization and the emission location are derived. The model predicts a phase lag between the observed polarization and intensity profiles, which is absent when the velocity correction due to corotation is ignored. For emission well within the light cylinder the model predicts an observed polarization angle curve which is very similar to a lagged version of the RVM polarization angle curve. We do not consider high-altitude emission since the electromagnetic fields near the light cylinder are unknown.

Assumptions about the symmetry of the emission region allow the emission radius to be inferred from polarization curves and intensity profiles. If the boundary of the emission region is symmetric with respect to the plane containing the spin and magnetic axes, the pulse phase midway between the outermost edges of the intensity profile arrives earlier than the pulse phase at which the position angle curve is steepest. The emission radius r is related to the time delay Δt via $r \approx c\,\Delta t/4$. Poorly constrained quantities, such as the angle between the spin and magnetic axes, do not enter the relation.

In an effort to present a specific example of the emission process, the implications of the model are studied within the context of coherent curvature emission. For emission in a narrow range of radii with a plasma distribution that is symmetric with respect to the magnetic axis the model predicts that observed intensity profiles should be asymmetric, with the leading half of the pulse brighter than the trailing half. This asymmetry has been observed. Of the 88 cone-dominated pulsars studied by LM88, 53 of the pulsars have a leading component that is clearly stronger than the trailing component, whereas the reverse is true for only 24 pulsars. An asymmetry of this sort has been predicted in another model which incorporates rotation (Chen & Shaham 1989) but the asymmetry predicted by their model is much smaller than the observed asymmetry for the small corotation speeds predicted by our model.

In § 3 we use the model to estimate the radius of radio emission for frequencies of 0.43 and 1.4 GHz. For 21 out of 23 objects we find that the radio emission originates at radii between 50 and 1000 km. For two objects, 1929+10 and 2110+27, the model predicts negative emission radii. Using additional data, we argue that the assumptions of a symmetric emission region with a dipolar magnetic field may be inappropriate for these objects.

The emission radii obtained are similar to other observational estimates of emission radius (Cordes 1978; Cordes, Weisberg, & Boriakoff 1983; Wolszczan & Cordes 1987; Smirnova & Shishov 1989; Phillips & Wolszczan 1990) and are within an order of magnitude or so of the various theoretical predictions (S71; RS75; Beskin, Gurevich, & Istomin 1986, hereafter BGI86; Cheng & Ruderman 1979, hereafter CR79). We find a marginal tendency for core emission to originate at smaller radii than cone emission, and a marginal tendency for emission height to increase with wavelength. The emission radii are used to put limits on the geometry of the emission region. We find that the assumption of a dipolar magnetic field with emission of field lines that pierce the light cylinder, is consistent with the data.

In § 4 we compare the relativistic flow model with the polarization models of Ferguson (1973), Shitov (1985), and Barnard (1986). Ferguson's model includes relativistic effects of second order but does not include relativistic effects of first order. Shitov's model depends on relativistic effects of third order, and predicts a lag between the polarization curve and the intensity profile of opposite sign to ours. Though Shitov presents some data which apparently support his model we find that the analysis technique used by him may be flawed. Barnard's model is dependent on the structure of the magnetic field at a substantial distance to the light cylinder, and the ambient plasma conditions there, both of which are unknown.

In § 5 we consider the possibility of a radius–to–pulse-width mapping in detail. Our results are consistent with such a mapping, but are at fairly serious odds with the recent affirmation by Rankin (1990) that core emission occurs at radii of nearly 10 km. We give another interpretation of the data used by Rankin, which incorporates a radius–to–pulse-width mapping in a natural way. In § 5 we also consider the possibility of a radius-to-frequency mapping.

As in Barnard's model, propagation effects may modify the predictions of the relativistic flow model. In § 6 we estimate the magnitude of propagation effects. The estimates require some assumptions about the magnetosphere, but within the context of our assumptions we find that propagation effects may be small enough to be ignored. Our conclusions are summarized in § 7.

2. THE RELATIVISTIC FLOW MODEL

2.1. *Particle Flow in a Rotating Dipolar Magnetic Field*

The model takes as its starting point the radiation produced by a relativistic particle moving in an arc (e.g., Jackson 1975). The particle beams its radiation in a narrow cone centered on the direction of its velocity. The radiation, integrated over angle and frequency, is polarized (87% linear) along the direction of the particle's acceleration. If one imagines that the pulsar radiation field is the sum of fields from many such particles (S71; RS75), then the emission from the plasma will be beamed along the velocity of the plasma and the radiation will be polarized along the direction of the acceleration of the plasma.

Plasma maser emission mechanisms in which the local Larmor frequency is large compared with the frequency of the maser radiation generally treat the radiating particles as "beads on a wire" (BGI86; CR79; Goldreich & Keeley 1971; Buschauer & Benford 1976, 1980; Melrose 1978), where the wire is a magnetic field line. For nonrotating conditions the magnetic field and its curvature determine the particle trajectories. The radiation modes are linearly polarized. The ordinary mode has its electric field in the plane spanned by the magnetic field and its curvature, while the electric field of the extraordinary mode is orthogonal to the magnetic field and its curvature. If the length scale for amplification is small compared with the light cylinder radius, the velocity and acceleration of the plasma should be used in place of the magnetic field direction and its curvature. The replacement of velocity by magnetic field, and acceleration by curvature are the new ingredients to the RVM that we include.

After being generated, the radiation propagates through the magnetosphere and reaches the interstellar medium. The observed radiation field will depend on the amount of refraction the radiation undergoes in the process (Melrose 1979; Arons & Barnard 1986, hereafter AB86; Barnard & Arons 1986, hereafter BA86) and on the rate at which ambient conditions change as the radiation propagates out of the magnetosphere (BRC75; Melrose & Stoneham 1977, hereafter MS77; CR79; Melrose 1979; Stinebring 1982). Any calculation of these propagation effects requires a model of the whole magnetosphere, and assumptions about emission locations. In the absence of a complete model of the magnetosphere and of a definite location for the emission, we cannot accurately include propagation effects, so they will be neglected in the derivation. The possible importance of propagation effects is discussed in § 6.

With the assumptions discussed above, the polarization is completely determined by the velocity and acceleration of the radiating particles. Consider the equation of motion for a single particle,

$$\frac{d\boldsymbol{p}}{dt} = q\left(\boldsymbol{E} + \frac{\boldsymbol{v}}{c} \times \boldsymbol{B}\right), \tag{1}$$

where $\boldsymbol{E}$ and $\boldsymbol{B}$ are the electric and magnetic fields acting on the particle, $\boldsymbol{p}$ and $\boldsymbol{v}$ are the momentum and velocity of the particle, q is the charge of the particle, t is time, and c is the speed of light, which will henceforth be set equal to unity. All quantities are measured in a Lorentz frame (i.e., an observer's frame). First assume that a velocity $\boldsymbol{v}_0$ exists such that the force vanishes. We take $v_0 \sim 1$. Let the radius of curvature of this trajectory be ρ, and let the true particle velocity be $\boldsymbol{v} = \boldsymbol{v}_0 + \boldsymbol{v}_1$, with $\boldsymbol{v}_1$ orthogonal to $\boldsymbol{B}$. Since the cyclotron frequency is assumed to be much larger than radio frequencies, the equation of motion may be averaged over a cyclotron orbit. This orbit is assumed to be negligibly small, so the acceleration of the plasma is the acceleration of the guiding center. Interesting these quantities into the Lorentz force formula and keeping leading order terms gives

$$m\gamma \frac{d\boldsymbol{v}_0}{dt} = q\boldsymbol{v}_1 \times \boldsymbol{B}, \tag{2}$$

where m and γ are the particle's mass and Lorentz factor. Inserting typical pulsar parameters (e.g., RS75) in equation (2) yields

$$v_1 \sim 2 \times 10^{-8} \gamma_3 r_8^3 \rho_8^{-1} B_{12}^{-1}. \tag{3}$$

In equation (3) and elsewhere, the stellar radius R_* is equal to 10 km, B_{12} is the surface dipolar magnetic field strength in units of 10^{12} G, ρ_8 and r_8 are the radius of curvature and the emission radius in units of 10^8 cm, and γ_3 is the Lorentz factor of the radiating electrons and positrons in units of 10^3. If force-free motion is possible ($E < B$, $\boldsymbol{E} \cdot \boldsymbol{B} = 0$), the flow will be very nearly force-free.

Calculations of the ambient conditions in the plasma outflow region (Arons & Scharlemann 1979; Arons 1983; Jones 1986; hereafter AS79, A83, and J86, respectively) indicate that the radio emission region may not be force-free and that electrons and positrons can be accelerated to energies of order 10^3 GeV. When force-free motion is not possible, the particle trajectories can be found approximately as long as the electric field is small compared with the magnetic field. Take a dipolar magnetic field with magnitude B_0 at the stellar surface. Let the angular frequency of the neutron star be Ω. We assume that particle energies are bounded by $e\Phi_{\max}$, where $\Phi_{\max} \sim B_0 \Omega^2 R_*^3$ is the maximum potential difference across the polar cap (GJ69; S71; RS75; BGI86). Additionally, we assume that the component of the electric field parallel to the magnetic field satisfies $E_\parallel \lesssim \Omega r B$, which is probably a significant overestimate. It is straightforward to show that[2]

$$\boldsymbol{v} = v_\parallel \boldsymbol{b} + \frac{\boldsymbol{E} \times \boldsymbol{B}}{B^2} + O[(\Omega r)^2]. \tag{4}$$

In equation (4), $\boldsymbol{b}$ is the magnetic field unit vector and $v_\parallel$ is the plasma velocity parallel to the magnetic field. As will be shown below, the correction term $O[(\Omega r)^2]$ is negligible within the context of our model.

The remaining problem is to find the large-scale electromagnetic fields in the near magnetosphere of the neutron star. If small-scale charge density and current density fluctuations (such as those necessary for radio emission!) are ignored, the fields and currents in the magnetosphere will vary periodically in time with the same period as the neutron star. Since the driving force of the system (the neutron star) is simply rotating, evolution in time by τ is equivalent to a rotation by $\Omega\tau$ (Mestel 1971). The time dependence of Ω due to spin-down of the pulsar is unimportant, since the spin-down time scale is huge compared with the rotation period. With this approximation, Maxwell's equations read (Mestel 1973):

$$\boldsymbol{E} + (\boldsymbol{\Omega} \times \boldsymbol{r}) \times \boldsymbol{B} = -\nabla\Phi, \tag{5a}$$

$$\nabla \cdot \boldsymbol{E} = 4\pi\rho, \tag{5b}$$

$$\nabla \times [\boldsymbol{B} - (\boldsymbol{\Omega} \times \boldsymbol{r}) \times \boldsymbol{E}] = 4\pi(\boldsymbol{J} - \boldsymbol{\Omega} \times \boldsymbol{r}\rho), \tag{5c}$$

$$\nabla \cdot \boldsymbol{B} = 0. \tag{5d}$$

The origin of coordinates is taken to be the center of mass of the neutron star. The accelerating potential, Φ, is assumed to be negligible inside the star and in any region with magnetic field lines that close within the volume $|\boldsymbol{\Omega} \times \boldsymbol{r}| < 1$ (GJ69; S71; RS75; BGI86). The boundary of this volume is the light cylinder with radius $R_{lc} = \Omega^{-1}$. The region threaded by magnetic field lines that do not remain within the light cylinder will be referred to as the open field line region.

For practical purposes we assume that the magnetic field near the star is well approximated by a dipole:

$$\boldsymbol{B}_0 = \frac{3\hat{\boldsymbol{r}}(\hat{\boldsymbol{r}} \cdot \boldsymbol{m}) - \boldsymbol{m}}{r^3}, \tag{6}$$

where $\boldsymbol{m}$ is the dipole moment of the star. This may not be accurate within a few stellar radii of the surface, since higher multipole components may be present, but the increased number of parameters associated with higher multiple components makes the application of the model untenable.

Assuming that equation (6) is reasonably accurate, the angular extent of the open field line region as a function of radius scales as $w \equiv (r\Omega)^{1/2} = (r/R_{lc})^{1/2}$ (GJ69; S71; RS75; M82; BGI83). The maximum potential available for accelerating particles is $\Phi_{\max} \sim m/R_{lc}^2$ (GJ69; S71; RS75; M82; BGI83). Taken together, these give $|\nabla\Phi|_{\max} \sim m/(rR_{lc})^{3/2}$, which is smaller than the corotation field, induced by B_0, by $O(w)$. Thus this term does not affect the direction of the plasma velocity to leading order and will be ignored.

In keeping with equation (4), equations (5c) and (5d) imply $\boldsymbol{J} = \rho\boldsymbol{\Omega} \times \boldsymbol{r} + f\boldsymbol{B}$, where f is a scalar function that is constant on magnetic field lines. Assuming $f_{\max} \sim \Omega$ (GJ69; S71; RS75; M82; BGI83; AS79; A38; J86), with $f = 0$ in the closed field line region, we obtain a correction to the dipole magnetic field

[2] Here and throughout the paper the symbol $O(x)$ corresponds to $O(x)$ as $x \to 0$. When used in vector equations, it refers to the magnitude of the correction.

$\delta B_{\max} \sim m(rR_{lc})^{-3/2}$. Corrections to the plasma velocity due to these polar currents will be $O(w^3)$. Like the corrections due to the accelerating potential, polar currents generate fields which modify the plasma velocity to higher order than first order in the corotation speed, and will be ignored. Thus, even for a dipolar stellar field and no propagation effects, the model includes an intrinsic uncertainty in the velocity of order w^3 which will propagate through all subsequent calculations. Fortunately, the corotation velocity is of order w^2, and, within the context of our assumptions, quantitative predictions of the model should be reliable for $w \ll 1$ (10% errors for emission at 1% of the light cylinder).

2.2. *Beaming Angles and Polarization*

In addition to the dipolar magnetic field, we assume an outflowing plasma with $\gamma \gg 1$. The plasma velocity is given by equation (4). Let α be the angle between the spin axis $\hat{z}$ and the dipole axis $\hat{\boldsymbol{m}}$ and let β be the angle between $\hat{z}$ and the line of sight $\hat{\boldsymbol{n}}$. A stationary right-handed coordinate system originating at the center of mass of the star is used and the origin of time is chosen so that $\hat{z}, \hat{\boldsymbol{m}}, \hat{\boldsymbol{n}}$ all lie in the $y = 0$ plane at $t = 0$,

$$\begin{aligned} \hat{\boldsymbol{m}} &= \hat{z} \cos \alpha + \sin \alpha(\hat{x} \cos \Omega t + \hat{y} \sin \Omega t) , \\ \hat{\boldsymbol{n}} &= \hat{z} \cos \beta + \hat{x} \sin \beta . \end{aligned} \tag{7}$$

The emission geometry is shown in Figure 1.

We assume that the emission comes from a single radius. For emission from one magnetic pole there is a single point on a sphere of the radius where particles beam along $\hat{\boldsymbol{n}}$ at any point in time. Complications due to a range of emission radii will be addressed in § 3. For kinematic purposes the speed of the outflowing plasma is equal to the speed of light, so the location of the emission point, $\boldsymbol{r}$, is determined by the equation

$$\hat{n} = \boldsymbol{\Omega} \times \boldsymbol{r} + \kappa \boldsymbol{b} . \tag{8}$$

In equation (8), κ is a constant which is found by demanding that the flow be away from the star. The angular extent of the open field line region is of order $w = (\Omega r)^{1/2}$; for emission within this tube the quantities $|\hat{\boldsymbol{n}} - \hat{\boldsymbol{m}}|$, $|\hat{\boldsymbol{n}} - \hat{\boldsymbol{r}}|$, and $|\hat{\boldsymbol{m}} - \hat{\boldsymbol{r}}|$ are all of order w. From the discussion in the previous section, the velocity given by equation (8) is trustworthy to second order in w, so the solution to equation (8) will be done to second order in w. With this limitation $\boldsymbol{\Omega} \times \boldsymbol{r} = r\boldsymbol{\Omega} \times [\boldsymbol{n} + (\hat{\boldsymbol{r}} - \hat{\boldsymbol{n}})] = r\boldsymbol{\Omega} \times \hat{\boldsymbol{n}} + O(w^3)$, which results in

$$\hat{\boldsymbol{n}} - r\boldsymbol{\Omega} \times \hat{\boldsymbol{n}} = \kappa \frac{3\hat{\boldsymbol{r}}(\hat{\boldsymbol{r}} \cdot \hat{\boldsymbol{m}}) - \hat{\boldsymbol{m}}}{[1 + 3(\hat{\boldsymbol{r}} \cdot \hat{\boldsymbol{m}})^2]^{1/2}} + O(w^3) . \tag{9}$$

Through third order in w, the left-hand side of equation (9) is a unit vector, so $\kappa = 1 + O(w^3)$. To solve this equation we take the dot product of equation (9) with $\hat{\boldsymbol{m}}$. This gives an algebraic equation for $\hat{\boldsymbol{m}} \cdot \hat{\boldsymbol{r}}$. Solving the algebra and substituting back into equation (9) gives $\hat{\boldsymbol{r}}$. The result is

$$\hat{\boldsymbol{r}} = \frac{2}{3}(\hat{\boldsymbol{n}} - r\boldsymbol{\Omega} \times \hat{\boldsymbol{n}})\left(1 + \frac{\epsilon^2}{18}\right) + \frac{\hat{\boldsymbol{m}}}{3}\left(1 + \frac{2\epsilon^2}{9}\right) + O(w^3) , \tag{10a}$$

$$\epsilon = [\sigma^2 + \sin \alpha \sin \beta(1 - \cos \Omega t)]^{1/2} + O(w^3) . \tag{10b}$$

In equation (10), ϵ is the angle between the magnetic axis and the line of sight, which takes on the minimum value σ. Define δ to be the angle between the emission point and the magnetic axis. If σ and Ωt are smaller than or of order $w^2 = \Omega r$, then

$$\delta = \tfrac{2}{3}\{\sigma^2 + [(\Omega t + \Omega r) \sin \alpha]^2\}^{1/2} + O(w^3) . \tag{11}$$

The magnetic azimuth, χ, is the angle between the components of $\hat{\boldsymbol{r}}$ and $\hat{z}$ that are orthogonal to the magnetic axis. With the constraints on σ and Ωt used in equation (11),

$$\sin \chi = \frac{2 \sin \alpha}{3\delta}(\Omega t + \Omega r) + O(w) . \tag{12}$$

If σ is sufficiently small, the minimum angle between the magnetic axis and the emission point occurs when $t \approx -r/c$, independent of α; the magnetic azimuth is antisymmetric about this same time. The result may be understood by noticing that, to first order, the left-hand side of equation (9) is $\hat{\boldsymbol{n}}$ rotated by an angle $-\Omega r$ about $\hat{z}$, and that this rotation is equivalent to a phase shift by $-\Omega r$.

Calculation of the position angle curve requires finding the acceleration of the plasma at the emission point. The projection of this acceleration on the plane of the sky is parallel to, or orthogonal to, the polarization direction. For $\boldsymbol{v} = \kappa \boldsymbol{b} + \boldsymbol{\Omega} \times \boldsymbol{r}$ the acceleration is

$$\boldsymbol{a} = \boldsymbol{\Omega} \times \boldsymbol{v} + \kappa \frac{d\boldsymbol{b}}{dt} + \boldsymbol{b} \frac{d\kappa}{dt} . \tag{13}$$

As shown above, $\kappa = 1$ through second order in w, so the derivative of κ in equation (13) will be set to zero. Substituting the unit vector for a dipolar magnetic field in equation (13) gives

$$\begin{aligned} \boldsymbol{a} = &-\frac{3}{2r}[\hat{\boldsymbol{r}} - \hat{\boldsymbol{n}}(\hat{\boldsymbol{n}} \cdot \hat{\boldsymbol{r}})] + \Omega \hat{z} \times \hat{\boldsymbol{n}} \\ &- \frac{1}{2}\left[\frac{\partial \hat{\boldsymbol{m}}}{\partial t} - \hat{\boldsymbol{n}}\left(\hat{\boldsymbol{n}} \cdot \frac{\partial \hat{\boldsymbol{m}}}{\partial t}\right)\right] + O\left(\frac{w^3}{r}\right) . \end{aligned} \tag{14}$$

The first term in equation (14) is obtained when rotation is ignored, while the second and third terms come from the corotation velocity and the partial derivative of the magnetic field with respect to time, respectively. The acceleration as a function of emission time is obtained from equation (14) using $\hat{\boldsymbol{r}}(t)$ from equation (10).

$$\boldsymbol{a} = -\frac{1}{2r}[\hat{\boldsymbol{m}} - \hat{\boldsymbol{n}}(\hat{\boldsymbol{n}} \cdot \hat{\boldsymbol{m}}) - 3\Omega r(\hat{z} \times \hat{\boldsymbol{n}})] + O\left(\frac{w^3}{r}\right) . \tag{15}$$

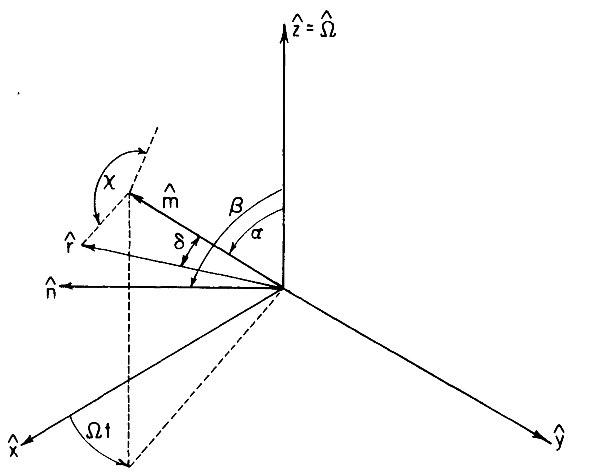

FIG. 1.—Emission geometry where $\hat{n}$ is toward the observer, $\hat{r}$ is toward the emission point, and $\hat{m}$ is the magnetic axis. The figure shown is for $\alpha = 45°$, $\sigma \equiv \beta - \alpha = 15°$, and $\Omega t = 10°$. The magnetic azimuth, χ, is negative as shown.

For the sake of definiteness, the radiation electric field is assumed to be along, rather than orthogonal to, the direction of the acceleration. The polarization angle will be defined as the angle between the radiation electric field and the projection of the spin axis on the plane of the sky:

$$\psi = \tan^{-1}\left[\frac{\sin\alpha\sin\Omega t - 3\Omega r\sin\beta}{\sin\sigma + \sin\alpha\cos\beta(1-\cos\Omega t)}\right]. \tag{16}$$

Up to this point all calculations have been done in terms of the emission time, the time of a given event as measured in a Lorentz frame in which the star's center of mass is at rest. For these results to apply to observations they must be expressed in terms of the reception time. For straight-line propagation at the speed of light, and a separation between source and receiver large compared with the size of the source, the time at which the radiation is received, t_r, depends on the emission time and the emission location via $t_r = t_e = \boldsymbol{r}(t_e)\cdot\hat{\boldsymbol{n}} + T_0$, where $\boldsymbol{r}$ is the emission location and T_0 is the travel time from the center of the star to the observer. To order w^3, $t_r = t_e - r + T_0$, so the conversion from time measured in the Lorentz frame to time measured by the observer is a constant offset, which we scale to zero.

If $\sigma \lesssim \Omega r$, the maximum derivative of the position angle curve with respect to time occurs when $\psi = 0$ at $t = 3r[1 + O(w)]$. Thus the model predicts that the center of the position angle curve lags the center of the δ curve by $\Delta t = 4r[1 + O(w)]$, as long as σ is sufficiently small. The result, $r_{\rm delay} = \Delta t/4$, will be referred to as the delay-radius relation.

In contrast to equation (16) the standard RVM equation is

$$\psi = \psi_0 + \tan^{-1}\left\{\frac{\sin\alpha\sin(\Omega t - \phi_0)}{\sin\sigma + [1-\cos(\Omega t-\phi_0)]\cos\beta\sin\alpha}\right\}, \tag{17}$$

where ψ_0 and ϕ_0 are the position angle offset and the center of the position angle curve, respectively. Within the accuracy of our calculation, equations (17) and (16) are equivalent with $\phi_0 = 3\Omega r$ and $\psi_0 = 0$. The shape of the observed ψ-curve is unchanged, e.g., the extremum value of $d\psi/dt$ is $\Omega\sin\alpha/\sin\sigma$ with the sign of the derivative equal to the sign of σ. First-order relativistic effects change only the relative phase of ψ and δ.

In addition to the analytical calculation, we explore the problem numerically. The simulations assume a dipolar magnetic field and a constant emission radius r. For a given emission time t_e the emission location $\boldsymbol{r}_e$ is found by solving equation (8) numerically. The accuracy is of the order of a microradian, which is much less than Ωr. The plasma acceleration at the emission point is obtained from direct, numerical calculation of equation (13), with time step $10^{-4}r$. The position angle is the angle between the acceleration and the projection of the spin axis on the plane of the sky, and the reception time is $t_r = t_e - \hat{\boldsymbol{n}}\cdot\boldsymbol{r}_e$. We find that the delay-radius relation holds, to within a few percent, if $\Omega r \lesssim 0.1$, even for $\sigma \sim w$.

Representative results of the simulations are shown in Figure 2. Notice that the ψ-curve lags the δ- and χ-curves and that the δ- and χ-curves are nearly symmetric and antisymmetric, respectively, about the same location in pulse phase. The input parameters for the figure are $\alpha = 45°$, $\beta = 40°$, and $\Omega r = 0.1$. The delay between the ψ- and δ-curves is 22°, whereas the delay-radius relation predicts a delay of 23°, giving a fractional error $\sim$4%. Fractional errors in this magnitude are typical for $\Omega r \lesssim 0.1$ and are negligible within the context of our assumptions.

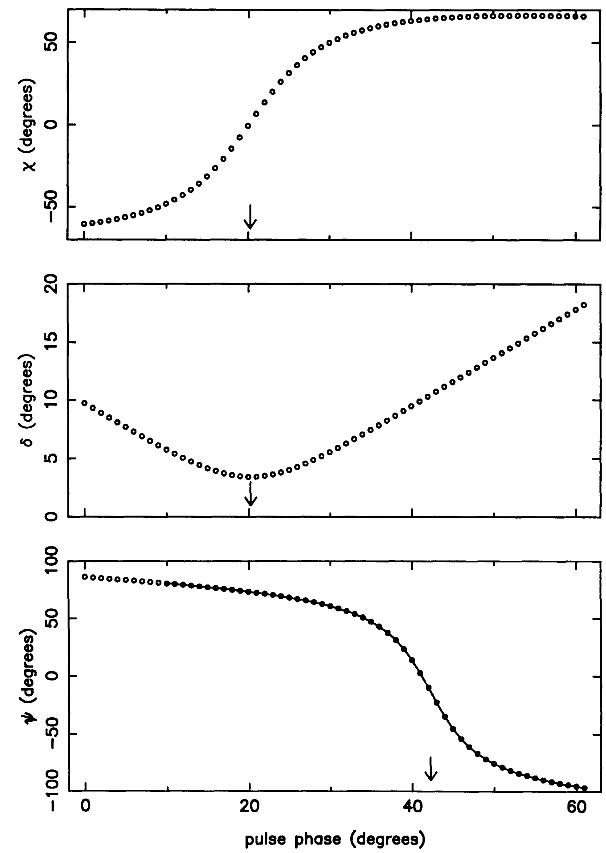

FIG. 2.—Representative curves of δ, χ, and the position angle ψ. The simulation used $\alpha = 45°$, $\beta = 40°$, and an emission height equal to 10% of the light cylinder radius. The circles are the results of a numerical simulation, with arrows pointing toward the symmetry or antisymmetry phases of the respective curves. The solid line on the bottom panel illustrates the region and the values of the least-squares fit of eq. (17) to the numerically obtained position angle curve. The rms error of the fit was 0°.02, and the value of σ from the fit was $-3°$.

The simulations show that relativistic effects steepen observed position angle curves for emission from field lines that bend toward the spin axis, and cause the observed position angle curves to be shallower for emission from field lines that bend toward the equatorial plane. A least-squares fit of equation (17) to the data of Figure 2 gives $\sigma = -3°$ instead of 5°. Since first-order, special relativistic effects do not change the extremum value of $d\psi/dt$, the change in slope is of higher than first order in Ωr. We will not consider these higher order corrections.

The delay-radius relation is not reliable for geometries where $\sin\beta \lesssim w$. This may be seen by noticing that the phase lag is a result of the corotation electric field. For noncorotation fields, the fractional error in emission radius estimates obtained using the delay-radius relation will depend on the ratio of the noncorotation field to the corotation field. This ratio is $\sim w/\sin\beta$, so for a small fractional error in emission radius estimates we need $w/\sin\beta \ll 1$.

2.3. *On the Relationship of Pulse Shape to the Open Field Line Region*

Even under the supposition of a single emission radius, use of the delay-radius relation requires that we also evaluate the pulse phase that corresponds to the minimum value of δ. The information available consists of total intensity, polarized intensity, and position angle as a function of pulse phase and observing frequency. These profiles are generated by plasma in the emission region, so it is necessary to understand the relationship between the location of the emission region and the magnetic field. It is generally agreed that the emission region lies in a region of outflowing plasma, which is qualitatively the same as the region threaded by magnetic field lines that pierce the light cylinder. For an aligned system with a purely dipolar magnetic field, the boundary of the open field line region is given by

$$\delta_{\max}^2 = \Omega r[1 + O(\Omega r)] , \qquad (18)$$

where $\delta_{\max}$ is the angle between the emission point and the magnetic axis for emission at the edges of the pulse. When $\sin \alpha \neq 0$, with a purely dipolar magnetic field, the open field line region is compressed in the meridional direction, but retains its symmetry in χ (Biggs 1990).

The actual boundary of the emission region is determined by plasma loss in the outer magnetosphere (GJ69; S71; RS75; M82), so an accurate determination of the emission region requires a complete model of the magnetosphere. We know of no model which consistently includes all of the effects we consider relevant to the problem (e.g., charge conservation). For the sake of definiteness, it is assumed that the flux-tube region is sufficiently symmetric in χ that the lag introduced by the flux tube's asymmetry in χ is small compared with Ωr.

If equation (18) is satisfied and the emission region fills the open field line region, the pulse width may be used to constrain the emission height (S71; RS75; Cordes 1978). In the limit that propagation effects are negligible, the pulse width W, emission radius, and geometrical factors obey

$$\frac{4}{9}\left(\sigma^2 + \frac{W^2}{4}\sin^2\alpha\right) = \Omega r . \qquad (19)$$

The geometric emission radii, $r_{\rm geo}$ obtained from equation (19) will be used to check the self-consistency of our model.

2.4. *Effects of Corotation Velocity on Beam Shape*

In an effort to present a specific example of pulsar radio emission, the implications of the relativistic flow model are considered within the context of curvature emission.

We approximate the power per unit frequency emitted by a particle of charge q moving along a path with radius of curvature ρ_c by

$$\frac{dP}{d\omega} = 0.517\,\frac{q^2}{\rho_c}\,(\omega\rho_c)^{1/3}\exp\left(-\frac{2\omega\rho_c}{3\gamma^3}\right). \qquad (20)$$

Equation (20) may be obtained by multiplicative interpolation of equations (14.93) and (14.94) in Jackson (1975), and has been employed in the study of curvature emission in the past (Buschauer & Benford 1976, 1980). For incoherent emission the power emitted per unit frequency per unit volume is obtained by multiplying equation (20) by the number density of the emitting particles, with appropriate averaging over particle Lorentz factors. As is well known, the radio emission from pulsars is not incoherent. For simplicity we assume that the emission is due to charge bunches that are small compared with the observing wavelength. For this case the emission per unit volume will be given by equation (20) multiplied by an effective charge density n.

We assume that the radiation is beamed directly along the velocity of the radiating particle velocity $\boldsymbol{v} = \kappa \boldsymbol{b} + \boldsymbol{\Omega} \times \boldsymbol{r}$. For a fixed radius and emission time the transverse area $A_\perp$ of the region beaming into our antenna is given by

$$A_\perp = r^2 \int H\left(1 - \frac{|\hat{v} - \hat{n}|}{\Delta\Sigma}\right) d^2\Sigma . \qquad (21)$$

In equation (21) $H(x)$ is the Heaviside function with $H(x) = 1$ for $x > 0$ and $H(x) = 0$ otherwise, $\Delta\Sigma$ is the solid angle subtended by the antenna as measured at the neutron star, and the integral is over solid angle. Evaluation of the integral is straightforward, with the result

$$A_\perp = \frac{4r^2\Delta\Sigma}{9}\,[1 + O(\Omega r) + O(\Delta\Sigma)] .$$

The received power per unit frequency for emission from a shell of thickness Δr is given by

$$P(t_r) = n\left.\frac{dP}{dw}\right|_{t_e} A_\perp \Delta r . \qquad (22)$$

In equation (22) t_r is the reception time and t_e is the associated emission time. The two were related via $t_r = t_e - r$. The radius of curvature is $\rho_c = a^{-1}$, where a is the magnitude of the acceleration at the emission point. The acceleration was obtained using equation (15) with $t = t_r + r$. The position angle was obtained using equation (17) with $t = t_r$ and $\phi_0 = 2\Omega r$. To minimize confusion over the origin of different effects, we take the number density to be $n = n_0 H(1 - \delta^2/\Omega r)$, with δ given by equation (11) with $t = t_r + r$. For simplicity we consider emission from a single radius. Some respective plots of the intensity and the position angle curve are shown in Figure 3.

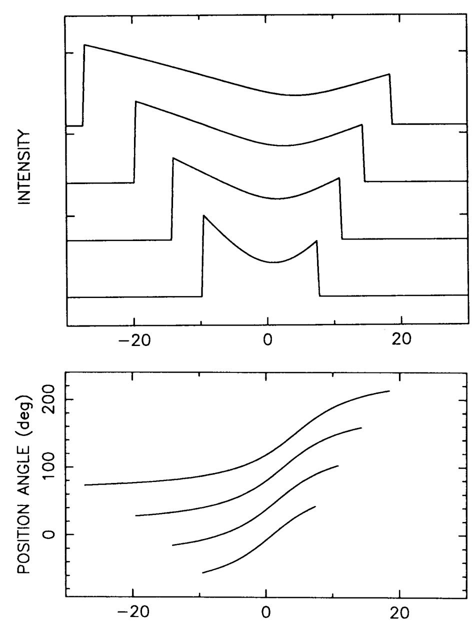

FIG. 3.—Representative plots of intensity and position angle vs. pulse for incoherent curvature radiation as discussed in § 2.4. The global input parameters for the curves are $\alpha = 45°$, $\sigma = 5°$, $\gamma = 700$, $P = 0.3$ s. The intensity profile at the top of the upper panel corresponds to the position angle curve at the top of the lower panel, and so on. The ordered pairs of emission radius (in km) and frequency (in GHz) are (*top to bottom*) (560, 0.01), (330, 01), (200, 1), (120, 10). The radius-to-frequency mapping used in the figure, $r \propto \nu^{-2/9}$, is discussed in § 5.2.

As is clear upon examining Figure 3, the corotation velocity tends to make the leading half of the pulse brighter than the trailing half. The effect is easily understood by considering equation (15). The minimum value of the acceleration at the emission point occurs when the position angle curve is steepest, at $t_r \approx 2r$. Since the emission per unit volume decreases as ρ_c increases, there is an associated dip in received intensity near $t_r = 2r$. On the other hand, the number density at the emission point is nearly symmetric about $t_r = -2r$, and as a result the intensity profile is skewed toward early times. The results of these simulations will be considered further in § 3.5.

The physical processes invoked to produce the asymmetric profiles shown in Figure 3 are different from the processes invoked to explain the cusped, high-energy profiles displayed by the Crab and Vela pulsars. The high-energy emission in these pulsars is thought to be produced at radii $\sim R_{1c}$, possibly near the boundary of the closed field line region (Cheng, Ho, & Ruderman 1986). The cusped shape of the observed profiles is usually ascribed to the shape of the emission region in conjunction with aberration effects.

In principle, the aberration effects invoked to model the high-energy emission in pulsars can be estimated using the techniques set forth in our paper, but it is by no means clear that our assumptions will hold for emission in the vicinity of the light cylinder. For radio emission at $r \ll R_{1c}$ the assumptions of our model appear perfectly reasonable. We now proceed to apply the relativistic flow model.

3. APPLICATION OF THE MODEL

In the section 23 pulsars are studied within the context of the relativistic flow model. The first section is concerned with the observing technique. The second section outlines our curve-fitting procedure and explains our method for determining the shift between the ψ- and δ-curves. In the third section individual objects are analyzed in light of our model. The fourth and fifth sections provide generalizations and discuss some implications of the model for the pulsar population. The last section discusses how emission radius relates to pulse morphology and other parameters.

3.1. *Data Acquisition*

Unless otherwise specified, the data were acquired at the Arecibo Observatory using the 40 MHz correlator as a multiplying polarimeter. The method is described briefly in Cordes, Wasserman, & Blaskiewicz (1990). Stokes parameters as a function of pulse phase and observing frequency were obtained from the various correlation functions, corrected for interstellar dispersion delay, and added together to yield minimally dispersed waveforms. A 20 MHz bandwidth was used for the 1.4 GHz data, and a 5 MHz bandwidth was used for the 0.43 GHz data. When low-frequency data using the technique described above were not available, the published data of Backer and Rankin (BR80) were used. General properties of the objects studied are shown in Table 1.

3.2. *Analysis Technique*

In this section the application of the relativistic flow model is developed. As mentioned in § 2, the position angle curves obtained in the simulations are very similar to time-lagged versions of the RVM. Thus position angle curves were fitted to the data using equation (17). To limit the effects of measurement errors, only those values of pulse phase for which the linearly polarized intensity L was at least 5 times its off-pulse rms were used. This gave a maximum statistical error of about

TABLE 1

GENERAL PROPERTIES OF OBJECTS STUDIED

Pulsar (1)	P (s) (2)	$\dot{P}$ (10^{-15} s s^{-1}) (3)	$(d\psi/d\phi)_{max}$ (deg deg^{-1}) (4)	$W_{10}(430)$ (5)	$W_{10}(1418)$ (6)
0301+19	1.38	1.30	−17	18°.5 ± 0°.2	15°.9 ± 0°.1
0525+21	3.74	40.06	+36	20.4 ± 0.1	18.4 ± 0.1
0540+23	0.24	15.43	−3	25.0 ± 0.3	23.9 ± 0.6
0611+23	0.25	59.63	+6	14.9 ± 0.4	18.2 ± 1.0
0751+32	1.44	1.07	+25	[a]	23.6 ± 0.6
0823+26	0.53	1.72	+18	9.6 ± 0.1	6.9 ± 0.1
0919+06	0.43	13.72	+8	18.6 ± 0.1	10.8 ± 0.3
0950+08	0.25	0.23	−2	36.6 ± 0.5	32.3 ± 0.1
1133+16	1.18	3.73	+10	12.4 ± 0.1	11.1 ± 0.1
1530+27	1.12	0.82	+5	14.8 ± 0.1	12.0 ± 0.3
1633+24	0.49	0.12	+6	36.9 ± 1	[a]
1737+13	0.80	1.45	−20	25.4 ± 0.4	22.1 ± 0.3
1839+09	0.38	1.09	−45	[a]	12.9 ± 0.3
1913+16	0.06	0.01	+51	60 ± 2	48.9 ± 0.1
1914+13	0.28	3.62	+41	[a]	12.0 ± 1
1915+13	0.19	7.20	−11	[a]	16.4 ± 1
1916+14	1.18	211	+43	[a]	6.6 ± 0.1
1924+16	0.58	0.22	+5	[a]	13 ± 1
1929+10	0.22	1.16	−1	20.9 ± 0.2	18.5 ± 0.1
1930+22	0.14	57.8	+7	[a]	14 ± 2
2110+27	1.20	2.62	−27	[a]	5.6 ± 0.3
2122+13	0.69	0.77	−13	16.0 ± 0.4	[a]
2210+29	1.00	0.49	−18	21.1 ± 0.4	[a]

[a] Data unavailable.

6° in the observed position angle curve. Some of the data were of high enough quality that the threshold was increased to 10 standard deviations. This cut the statistical error in half, and excluded data for which errors in the unpulsed components of the Stokes parameters could produce significant systematic errors.

Additional segments of some polarization curves were excluded because of the presence of dual polarization modes, and the reasons for these excisions will be given in the discussions of the individual objects. After removal of the questionable data, equation (17) was fitted to the remaining data using least squares. The fit weighted all the remaining data equally. We chose uniform weighting, since departures of the data from equation (17) need not be solely statistical in nature. The resulting fits were very good for some objects, with a root mean square error on the order of degrees. For a few objects the fits were poor. Within the context of the model this could be due to strong nondipolar components of the stellar magnetic field or to our inability to recognize all regions of orthogonal moding in the data.

Table 2 displays the geometric fit parameters, defined in § 2.2, for the objects which were fitted well by equation (17). Columns (3) and (4) give the optimal values of the angle between the spin axis and the magnetic axis α and the minimum angle between the magnetic axis and the line of sight σ; column (6) gives the value of σ obtained when α is fixed at 45°; and the root mean square (rms) values of the residuals for the optimal fits are shown in column (5). The errors quoted in the table were obtained by linearizing the fitting function in the vicinity of minimum chi-square and employing the results of linear least-squares theory (e.g., Jenkins & Watts 1968). For all the objects the optimal values of α and σ at 0.43 GHz and 1.4 GHz are the same within 1 standard deviation. However, for for a given object the values of σ_{45} at 0.43 GHz and 1.4 GHz often differ by more than 1 standard deviation. The variations in σ_{45} may be due to systematic deviations of the data from equation (17).

As a test of the applicability of equation (17), the position angle curve was decomposed into parts that were symmetric and antisymmetric about the center of the fit ϕ_0. We find that the rms of the symmetric part of the ψ-curve is usually consistent with the expected value for additive noise, so at our level of signal-to-noise an antisymmetric position angle curve is consistent with most of the data. The rms values of the fit residuals are larger by about a factor of $(2)^{1/2}$ than can be expected by additive noise alone, so there may be a systematic departure of the data from equation (17). Given that the errors in the fit parameters were estimated using the fit residuals, instead of the expected statistical error, any systematic departures from equation (17) are included in the error estimates.

As discussed in § 2, it is assumed that the minimum value of the angle between the emission point and the magnetic axis δ occurs when the emission originates closest to the center of the open field line region, so the location of the region must be related to a fiducial phase of the intensity profile. Work on pulsar beam shapes (LM88) indicates that beam components may be located asymmetrically within the open flux tube. Estimators of the profile center that depend on the value of the intensity in a fundamental way, such as the phase of peak intensity or the pulse phase corresponding to the median of the intensity distribution, may therefore be misleading. If the emission region fills the flux tube, and the emission radius is constant, the pulse phase corresponding to the minimum value of δ will be midway between the outer edges of the intensity profile. A large range of emission radii make a measurement of this kind difficult to interpret, but the same shortcoming appears to be present in all techniques. Thus it is assumed, as a working hypothesis, that the emission comes from a single radius and that this emission fills the flux tube.

The center of the flux tube, ϕ_1, is identified with the pulse phase midway between the outermost edges of the pulse intensity profile. This pulse phase was found by identifying the first and last pulse components by eye (these are the same for the component), finding the 10% outer edges for each peak, taking the average value, and repeating this for smaller percentages. The center of the flux tube, ϕ_1, was usually identified with an intensity level of 2%, but poor signal-to-noise or shallow intensity gradients sometimes required using the 5% or 10% intensity levels. The value of I between bins was obtained via linear interpolation. Errors in ϕ_1 were estimated by assuming that the errors in the edge estimates were independent and satisfied $\sigma(\phi) \approx 2\sigma(I)/|dI/d\phi|$, where $\sigma(I)$ was the rms of the off-pulse noise and $dI/d\phi$ was the derivative of the waveform in the vicinity of the edge.

In general, the calculation of quantities based on a percentage of the maximum flux requires a knowledge of the absolute flux (e.g., the unpulsed component). Since this value is unknown, it is useful to define the pulse center in a baseline-independent way. Toward this end, three additional estimates of the pulse center were used. The first, ϕ_2, corresponds to the pulse phase which maximizes the quantity,

$$\int [I(\phi - \phi_2) + I(\phi_2 - \phi)]^2 \, d\phi \, .$$

Errors in ϕ_2 were estimated by fitting a parabola to the values of the integral in the vicinity of the maximum and finding the error in the location of the peak using linearized least squares.

The third estimator, ϕ_3, is the pulse phase which corresponds to the median phase when the intensity, over a single period, is taken as a distribution. Errors in ϕ_3 were estimated using a technique like that used to find the errors in ϕ_1, with the intensity replaced by the integral of the intensity.

The final estimator, ϕ_4, is the pulse midway between the locations in pulse phase where the intensity rises above the period average intensity, and the errors were estimated as in ϕ_1. All four estimators give the same location in pulse phase for symmetric intensity profiles. Table 3 shows the various phase-delay estimates, $\Delta\phi_i = \phi_0 - \phi_i$, and gives our best values for $r_{\rm delay}$. Values of $r_{\rm geo}$ obtained using the 10% pulse widths are shown in column (8) of Table 3. The data and fits are shown in Figures 4–26, with the center of the pulse intensity profile and ϕ_0 marked by arrows. The vertical bars on the intensity plots mark the pulse edges. The error in the pulse center is approximately the error associated with the 10% width, given in Table 1. The small parameter w may be obtained from $w \sim (\Delta\phi/4)^{1/2}$ with appropriate unit conversions.

3.3. *Individual Objects*

In this section we discuss the individual characteristics of 23 pulsars for which we have good polarization data, and which have ψ-curves that are fitted well by equation (17). In an effort to present a general picture of the objects, we use the empirical classification scheme of Rankin (1983, 1986, 1990, hereafter R83, R86, R90).

TABLE 2

FITTING PARAMETERS

Pulsar (1)	Observing Frequency (MHz) (2)	α (deg) (3)	σ (deg) (4)	rms Residuals (deg) (5)	σ_{45} (deg) (6)
0301+19..........	430	119 ± 30	−2.8 ± 0.4	1.6	−2.44 ± 0.03
	1418	111 ± 16	−2.9 ± 0.3	2.0	−2.32 ± 0.03
0525+21..........	430	40 ± 9	1.0 ± 0.2	0.6	1.11 ± 0.01
	1418	46 ± 10	1.2 ± 0.2	2.0	1.17 ± 0.02
0540+23..........	430	125 ± 12	−14 ± 1	1.2	−12.6 ± 0.4[a]
	1418	163 ± 40	−5 ± 10	1.5	−11.0 ± 0.4[a]
0611+22..........	430	17 ± 160	4 ± 40	2.0	8.0 ± 0.6
	1418	150 ± 100	6 ± 15	2.2	6.4 ± 0.3
0751+32..........	1418	78 ± 33	2.4 ± 0.5	2.9	1.6 ± 0.1
0823+26..........	430	79 ± 1	3.2 ± 0.3	5.6	1.9 ± 0.2
	1418	91 ± 600	3 ± 1	1.5	2.2 ± 0.1
0919+06..........	430	45 ± 200	5 ± 16	1.3	4.5 ± 0.3
	1418	90 ± 100	8.6 ± 0.6	3.1	6.0 ± 0.3
0950+08..........	430	6 ± 90	−2.5 ± 40	3.9	−16.5 ± 0.5
	1418	6 ± 30	−2.5 ± 15	3.4	−16.6 ± 0.2
1133+16..........	430	35 ± 50	3 ± 4	0.5	4.1 ± 0.1
	1418	147 ± 110	3 ± 10	1.8	4.4 ± 0.1
1530+27..........	430	48 ± 280	8 ± 35	1.6	7.7 ± 0.5
	1418	33 ± 1000	6 ± 100	1.3	7.4 ± 0.6
1633+24..........	430	150 ± 120	5 ± 20	5.0	7.1 ± 0.2
1737+13..........	430	7 ± 270	−0.3 ± 12	5.8	−21 ± 0.2
	1418	6 ± 260	−0.3 ± 13	3.9	−1.9 ± 0.1
1839+09..........	1418	34 ± 400	−1 ± 8	15	−0.9 ± 0.2
1913+16..........	430	127 ± 5	1.0 ± 0.1	2.5	1.0 ± 0.1[a]
	1403	171 ± 64	0.2 ± 1	2.7	0.6 ± 0.1[a]
1914+13..........	1418	66 ± 200	1.3 ± 2	3.5	1.0 ± 0.1
1915+13..........	1418	94 ± 24	−5.4 ± 0.2	0.8	−3.7 ± 0.1
1916+14..........	1418	13 ± 100	0.3 ± 2	1.3	0.85 ± 0.01
1924+16..........	1418	100 ± 600	12 ± 40	2.1	7.7 ± 0.5
1929+10..........	430	155 ± 2	−16 ± 2	4.0	−26 ± 2[a]
	1418	153 ± 4	−16 ± 3	4.1	−26 ± 4[a]
	1418[b]	30 ± 10	3 ± 2	2.9	
1930+22..........	1418	50 ± 300	6.2 ± 25	0.9	6.2 ± 0.2
2110+27..........	1418	43 ± 800	−1.5 ± 20	0.7[c]	−1.5 ± 0.01
2122+13..........	430	90 ± 60	−4 ± 2	2.7	−3.1 ± 0.1
2210+29..........	430	50 ± 50	−3 ± 2	4.7	−2.3 ± 0.1

[a] Used $\alpha = 135°$.
[b] Alternative fit parameters; see text discussion of 1929+10.
[c] Far less than expected, see text discussion of 2110+27.

TABLE 3

Phase Lag and Emission Radius Estimates

Pulsar (1)	Observing Frequency (MHz) (2)	$\Delta\phi_1$ (deg) (3)	$\Delta\phi_2$ (deg) (4)	$\Delta\phi_3$ (deg) (5)	$\Delta\phi_4$ (deg) (6)	r_{delay} (km) (7)	r_{geo} (km) (8)
0301+19..........	430	0.65 ± 0.2	0.8 ± 0.1	−0.9 ± 0.1	[a]	180 ± 60	700^{+140}_{-240}
	1418	0.2 ± 0.1	0.1 ± 0.1	−0.9 ± 0.1	0.25 ± 0.4	60 ± 30	550^{+100}_{-200}
0525+21..........	430	0.3 ± 0.1	0.45 ± 0.1	3 ± 1	0.4 ± 0.1	230 ± 80	1200^{+300}_{-300}
	1418	0.4 ± 0.2	0.3 ± 0.1	−1 ± 2	0.4 ± 0.3	300 ± 150	1000^{+250}_{-250}
0540+23[b].........	430	17 ± 2	24 ± 2	25 ± 2	18 ± 2	850 ± 100	230 ± 200
	1418	11 ± 2	17 ± 2	17 ± 2	11 ± 2	550 ± 100	220 ± 200
0611+22..........	430	6 ± 2	6 ± 2	6 ± 2	6 ± 2	300 ± 100	250[c]
	1418	7 ± 2	7 ± 2	7 ± 2	7 ± 2	350 ± 100	300[c]
0751+32..........	1418	0.8 ± 0.6	1.4 ± 0.6	3.3 ± 0.6	[d]	240 ± 180	1300^{+60}_{-600}
0823+26..........	430	1.5 ± 1	0.8 ± 1	1.2 ± 1	1.5 ± 1	150 ± 100[e]	100^{+10}_{-10}
	1418	1.5 ± 1	1.3 ± 1	1.5 ± 1	1.5 ± 1	150 ± 100[e]	70^{+10}_{-10}
0919+06[b].........	430	8.5 ± 1.5	5.7 ± 1.5	6.5 ± 1.5	8.5 ± 1.5	760 ± 140	390[c]
	1418	4 ± 2	1.5 ± 2	2 ± 2	4 ± 2	360 ± 200	230[c]
0950+08..........	430	12.5 ± 1.5	3.4 ± 1	5 ± 1.5	11 ± 4	600 ± 200[e]	20^{+600}_{-20}
	1418	16.5 ± 1.5	4 ± 1	5 ± 1.5	8 ± 2	600 ± 200[e]	20^{+600}_{-20}
1133+16..........	430	0.2 ± 0.7	0.6 ± 0.7	1.7 ± 0.7	[a]	250 ± 250	600[c]
	1418	2.4 ± 0.5	2.9 ± 0.5	4.6 ± 0.5	2.6 ± 0.5	250 ± 250	500[c]
1530+27[b].........	430	4 ± 4	4 ± 4	4 ± 4	4 ± 4	700 ± 1000	1200[c]
	1418	−3 ± 10	−3 ± 10	−3 ± 10	−3 ± 10	700 ± 1000	1100[c]
1633+24..........	430	7 ± 2	15 ± 2	15 ± 2	[d]	700 ± 200	1400[c]
1737+13..........	430	1.2 ± 0.5	4.5 ± 0.2	1.4 ± 0.2	2.5 ± 0.2	420 ± 170	900[c]
	1418	1.4 ± 0.4	2.5 ± 0.2	3.8 ± 0.2	2.3 ± 0.2	380 ± 170	700[c]
1839+09..........	1418	1.7 ± 1	1.9 ± 04	2.1 ± 0.4	[d]	160 ± 80	100[c]
1913+16..........	430	8.7 ± 1.3	11.1 ± 0.1	10.1 ± 0.1	[d]	156 ± 12	200 ± 100
	1418	12.8 ± 0.2	13.2 ± 0.2	5.8 ± 0.1	12.8 ± 0.5	156 ± 12	130 ± 50
1914+13..........	1418	2.3 ± 0.5	2.3 ± 0.2	2.6 ± 0.2	[d]	140 ± 30	70[c]
1915+13[b].........	1418	5.5 ± 1	6.0 ± 1	6.8 ± 1	5.7 ± 1	240 ± 80	120[c]
1916+14..........	1418	0.2 ± 0.2	0.1 ± 0.1	0.6 ± 0.3	[d]	100 ± 100	100[c]
1924+16[b].........	1418	5.5 ± 15	4.6 ± 15	5 ± 15	[d]	600 ± 1800	600[c]
1929+10..........	430	−15 ± 1	−15 ± 1	−14 ± 1	−15 ± 1	[f]	570 ± 60
	1418	−15 ± 1	−15 ± 1	−15 ± 1	−15 ± 1	[f]	560 ± 60
1930+22..........	1418	4.4 ± 5	6 ± 5	6 ± 5	[d]	150 ± 150	110[c]
2110+27..........	1418	−2.6 ± 1.2	−2.3 ± 1	−2 ± 1	−2.5 ± 1.5	[f]	100[c]
2122+13..........	430	0.8 ± 0.5	0.3 ± 0.3	1.2 ± 1	0.3 ± 2	100 ± 70	400[c]
2210+29..........	430	1.4 ± 1	1.3 ± 1	2.2 ± 1	[d]	290 ± 200	800[c]

[a] Data from BR80; no off-pulse data given.
[b] Could be one-sided conal; see § 3.5.
[c] α unconstrained; used $\alpha = 90°$, giving an approximate upper limit.
[d] Meaningless due to poor signal-to-noise.
[e] Very uncertain; see text.
[f] No estimate made; see text.

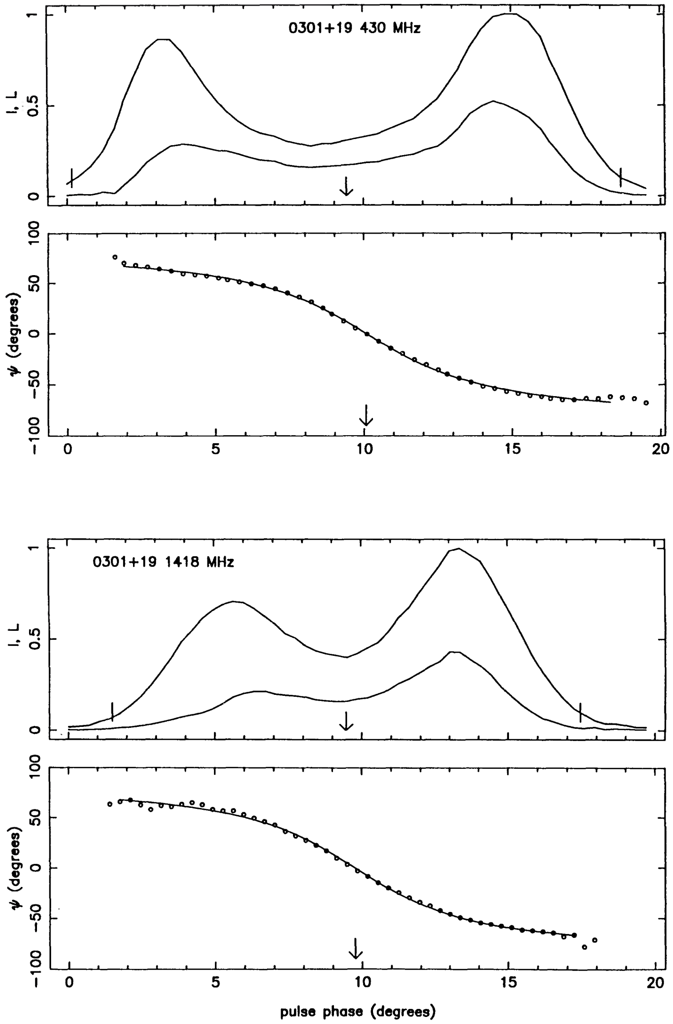

FIG. 4.—Total intensity, linearly polarized intensity, and position angle for 0301 + 19 at two frequencies. The 430 MHz emission is from BR80. The region of pulse-phase fit by eq. (17) is shown by the smooth curve. The pulse center marked by the arrow in the top panel is the pulse phase midway between the 10% intensity levels. The vertical bars mark the pulse edges that were used. The arrow on the position angle curve points to the maximum gradient in the fitted position curve.

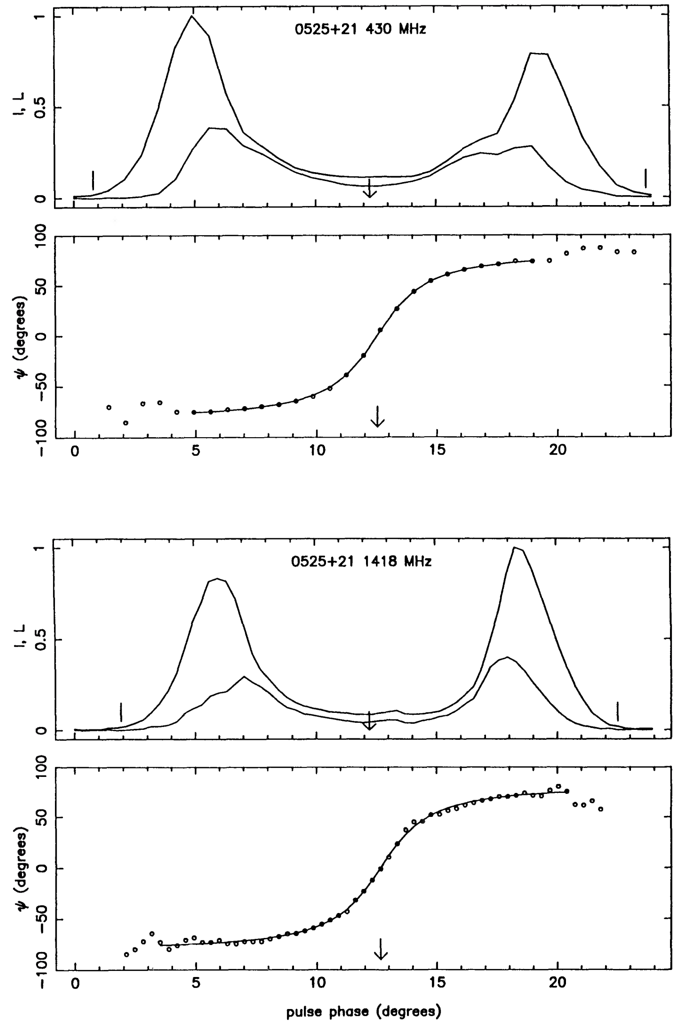

FIG. 5.—Total intensity, linearly polarized intensity, and position angle for 0525 + 21 at two frequencies. The region of pulse-phase fit by eq. (17) was slightly narrowed because of orthogonal moding (S84a, b). The pulse center marked by the arrow in the top panel is the pulse phase midway between 2% intensity levels. The arrow on the position angle curve points to the maximum gradient in the fitted position angle curve.

3.3.1. *0301 + 19*

This object is a conal double (R83; R90). The bridge of emission between the two peaks exhibits a somewhat redder fluctuation spectrum than the two peaks (Schönhardt & Sieber 1973). In the time domain this means that the pulse-to-pulse intensity in the bridge is correlated over a longer time than the pulse-to-pulse intensity in the two peaks. The difference in the correlation functions indicates that the bridge emission may originate in a different location than the peaks. The obvious asymmetry in the profile offsets the phase-lag estimates $\Delta\phi_2$ and $\Delta\phi_3$ toward the stronger component, so $\Delta\phi_1$ and $\Delta\phi_4$ were used to estimate r_{delay}.

3.3.2. *0525 + 21*

Like 0301 + 19, the bridge of emission in this conal double (R83; R90) profile has different fluctuation properties from the peaks (Backer 1973). The presence of an offset core component will cause the phase-lag estimates $\Delta\phi_2$ and $\Delta\phi_3$ to be offset from the center of the pulse, so the other two estimates were used to obtain the emission radius. The measured phase lags for this object are extremely small, and thus even a small quadrupole component in the stellar magnetic field could introduce substantial errors in the emission radius estimates.

3.3.3. *0540 + 23*

This object has been tentatively classified as a core single (R86; R90). It is often the case that core emission does not exhibit polarization angle curves that are in accord with the rotating vector model (R83; R90), but it does not appear to be the case for this object. However, the obvious asymmetry of the profile does suggest that the emission region may not be symmetric with respect to the magnetic axis. This possibility is reinforced by the fact that the difference in r_{relay} between the 1.4 GHz emission and the 0.43 GHz emission is the order 400 km when the median of the profile is taken to be the peak of the emission. This is significantly larger than the 300 km difference

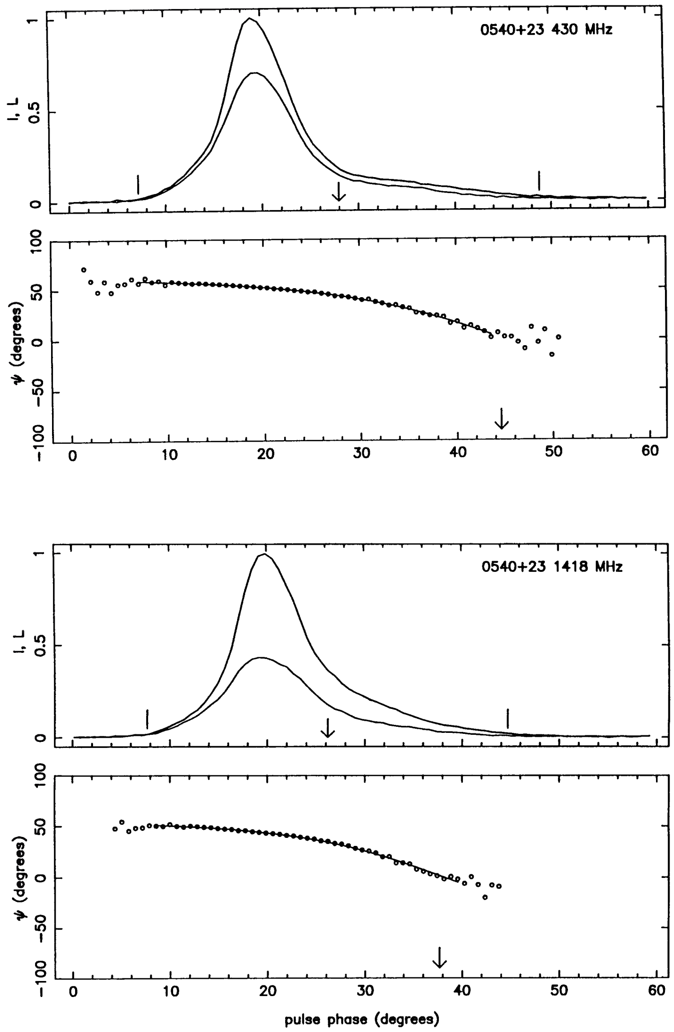

FIG. 6.—Total intensity, linearly polarized intensity, and position angle for 0540+23 at two frequencies. All values of pulse phase with linearly polarized intensity in excess of 10 times its off-pulse rms were used in the fit. The pulse center marked by the arrow in the top panel is the pulse phase midway between the 2% intensity levels. The arrow on the position angle curve points to the maximum gradient in the fitted position angle curve.

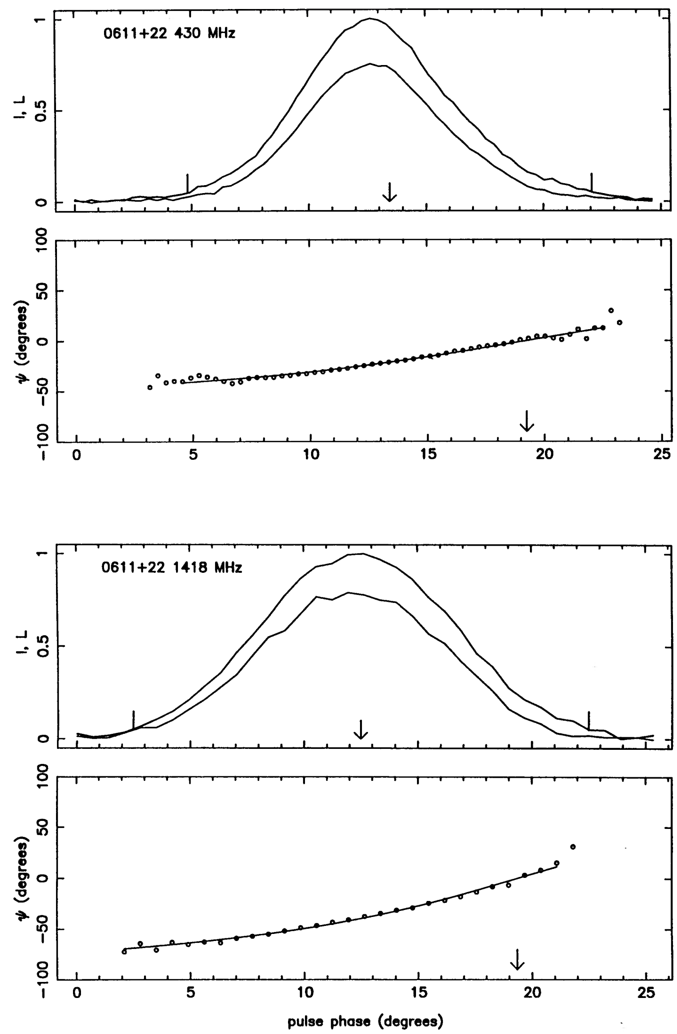

FIG. 7.—Total intensity, linearly polarized intensity, and position angle for 0611+22 at two frequencies. All values of pulse phase where the value of linearly polarized intensity was 5 times its off-pulse rms were used in the fit. All measurements of pulse center were the same within measurement errors. The pulse center marked by the arrow in the top panel is the pulse phase midway between the 5% intensity levels. The arrow on the position angle curve points to the maximum gradient in the fitted position angle curve.

quoted in Table 2. If the peak is associated with emission from one side of a conal beam, the discrepancy could be due to the bending of the flux tube with radius, in conjunction with the delay-radius relation. Thus the results in Table 2 must be considered as tentative. Additional discussion of the object may be found in § 3.5.

3.3.4. *0611+22*

This object has also been tentatively identified as a core single (R86), with some unusual characteristics. Integrations of a few pulses show that the pulse arrival times tend to wander around the arrival times predicted by a smooth spin-down model by 800 μs over time scales of order 10 minutes (Ferguson & Boriakoff 1980). Given estimates of the plasma conditions near a neutron star (RS75; S71), it is likely that the emission region is well inside the Alfvén radius. Hence this wandering of the pulse is probably due to changing plasma emission and not due to wandering field lines. The 1.4 GHz profile is wider than the 0.43 GHz profile, which suggests that the emission radius increases with frequency, or that the 1.4 GHz profile is broadened by the presence of conal emission. The phase lags argue for increased emission radius with frequency, but the errors are large enough to allow for the reverse.

3.3.5. *0751+32*

This object is a conal double (R83; R90). The position angle data on the leading edge of the pulse were excluded from the fit because of the obvious jump in position angle. We chose ϕ_1 as the best estimate of the pulse center because of the asymmetry of the intensity profile and the level of signal-to-noise.

3.3.6. *0823+26*

The main pulse of 0823+26 is due to core emission (R90). This object exhibits significant orthogonal moding both before and after the main pulse, at both 0.43 and 1.4 GHz. Backer & Rankin (BR80) found that the position angle data could be fitted by assuming that the emission was the incoherent superposition of two modes, each of which was characterized by a

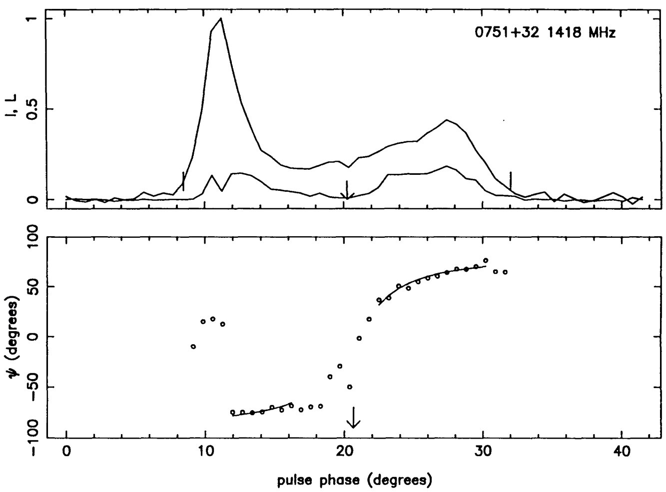

FIG. 8.—Total intensity, linearly polarized intensity, and position angle for 0751+32 at 1418 MHz. The 10% edges of the intensity profile are shown. The arrow on the position angle curve points to the maximum gradient in the fitted position angle curve.

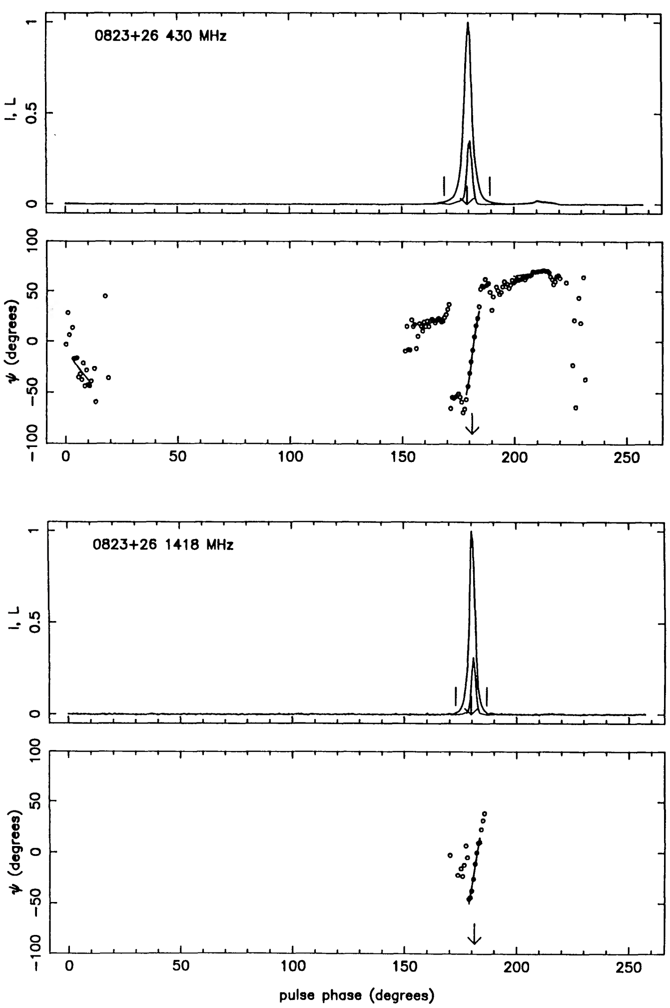

FIG. 9.—Total intensity, linearly polarized intensity, and position angle for 0823+26 at two frequencies. Significant orthogonal moding exists at both frequencies (S84a; BR80), and regions where it is present were not included in the fits. The pulse center marked by the arrow in the top panel is the pulse phase midway between the location where the intensity rises above average. The arrow on the position angle curve points to the maximum gradient in the fitted position angle curve.

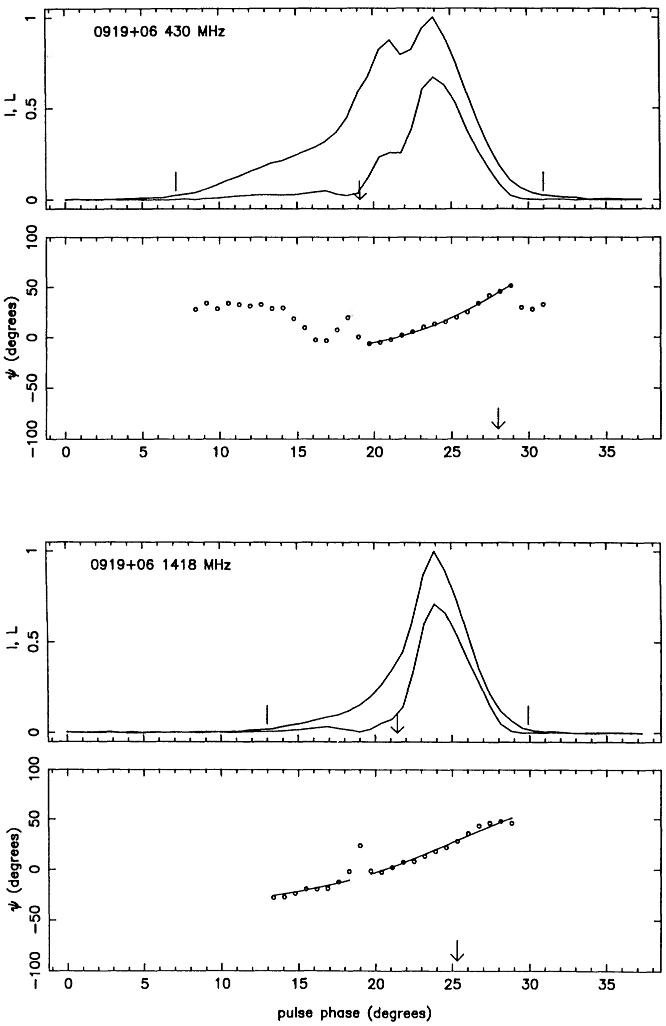

FIG. 10.—Total intensity, linearly polarized intensity, and position angle curve for 0919+06 at two frequencies. Significant orthogonal modeling exists on the leading edge of the 430 MHz profile. The 2% intensity levels are indicated.

(different) RVM. There does not seem to be any way to incorporate their procedure into our model. Significant asymmetry in the field or the open field line region seems likely for this object. The emission radius was determined using only the main pulse, whose center was estimated using ϕ_1 and ϕ_4, with formal errors. The estimate of $r_{\rm delay}$ is very uncertain, but the fit parameters obtained using the data at 0.43 GHz are well constrained and are consistent with previous results (LM88).

3.3.7. *0833−45*

An excellent polarization profile and a fit of the RVM for 0833−45 is shown in Figure 11 of Krishnamohan & Downs (1983, hereafter KD83). From Figure 11 of KD83 we estimate the maximum position angle gradient to occur at 7°.5. Such an estimate would be *very* difficult if the position angle gradient were not plotted. The pulse edges are difficult to judge by eye, so we estimate the pulse center using the 10% intensity levels. We find the pulse center to be at about 6°.5. A phase lag of 1°, with a period of 0.09 s gives a fiducial emission radius of 20 km for 0833−45. We note that equation (17) does not fit the data very well, and that the departure of the data from equation (17) is not obvious without the aid of a fit.

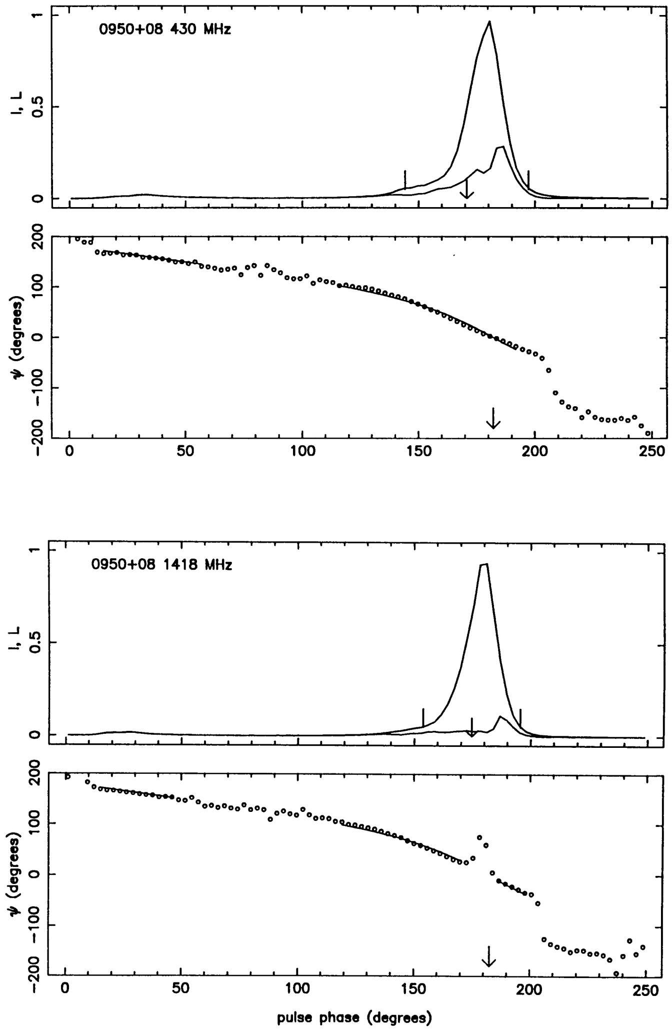

FIG. 11.—Total intensity, linearly polarized intensity, and position angle curve for 0950+08. Significant orthogonal moding exists at 1418 MHz (S84a), which is a reason for the excluded region in the fit. The pulse center marked by the arrow in the top panel is the pulse phase midway between the locations where the intensity rises above average. The arrow on the position angle curve points to the maximum gradient in the fitted position angle curve.

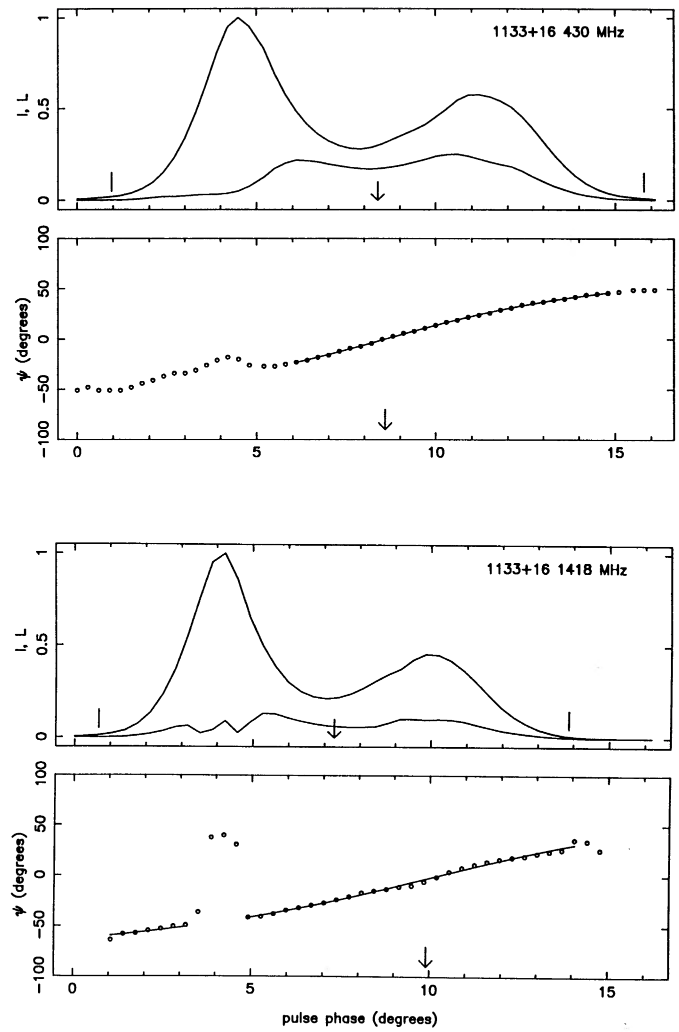

FIG. 12.—Total intensity, linearly polarized intensity, and position angle for 1133+16 at two frequencies. Significant orthogonal moding exists at 430 MHz (BR80) and probably at 1418 MHz. Regions where it is thought to be strong were not included in the fits. The pulse center marked by the arrow in the top panel is the pulse phase midway between the 2% intensity levels. The arrow on the position angle curve points to the maximum gradient in the fitted position angle curve.

3.3.8. *0919+06*

The 0.43 GHz profile suggests that this pulsar has three components, and observations over a broader frequency range bear this out (R90). Single-pulse observations show little orthogonal moding at 1.4 GHz (S84a), but the obvious difference between the 0.43 and 1.4 GHz position angle curves suggests that the leading edge of the 0.43 GHz profile is in the orthogonal mode. The asymmetry of the profile argues that ϕ_1 and ϕ_4 are the best estimates of the pulse center, and these were used to estimate $r_{\rm delay}$. Additional discussion of this object may be found in § 3.5.

3.3.9. *0950+08*

The optimal value of α in Table 2 suggests that this object is nearly aligned. Other analyses of this pulsar (Manchester & Lyne 1977; Hankins & Cordes 1981; NV83; LM88) also imply a nearly aligned system, with emission coming from a single magnetic pole, on field lines that initially bend toward the spin axis. If this is true, the interpulse implies that the beam must be fanned out in the longitudinal direction, which is consistent with the classification of both the main and interpulses as conal single profiles (R90).

The pulse widths in Table 1 are fairly large, and could be larger than α, so the validity of the delay-radius relation is questionable for this object. The asymmetry of the main pulse suggests that ϕ_1 and ϕ_4 are the best estimates of the phase delay, and these estimates do not agree. The values of $r_{\rm delay}$ quoted were obtained by averaging $\Delta\phi_1$ and $\Delta\phi_4$ for both frequencies. The errors were taken to encompass the range of the phase-delay values. The $r_{\rm delay}$ estimates for this object are also questionable.

3.3.10. *1133+16*

This conal double profile exhibits orthogonal moding near the first peak at 1.4. GHz (S84a), and also near the second peak at 0.43 GHz (BR80). Additionally, 1133+16 has a fairly shallow position angle excursion. For these reasons, the value of ϕ_0 obtained by fitting equation (17) may have little to do

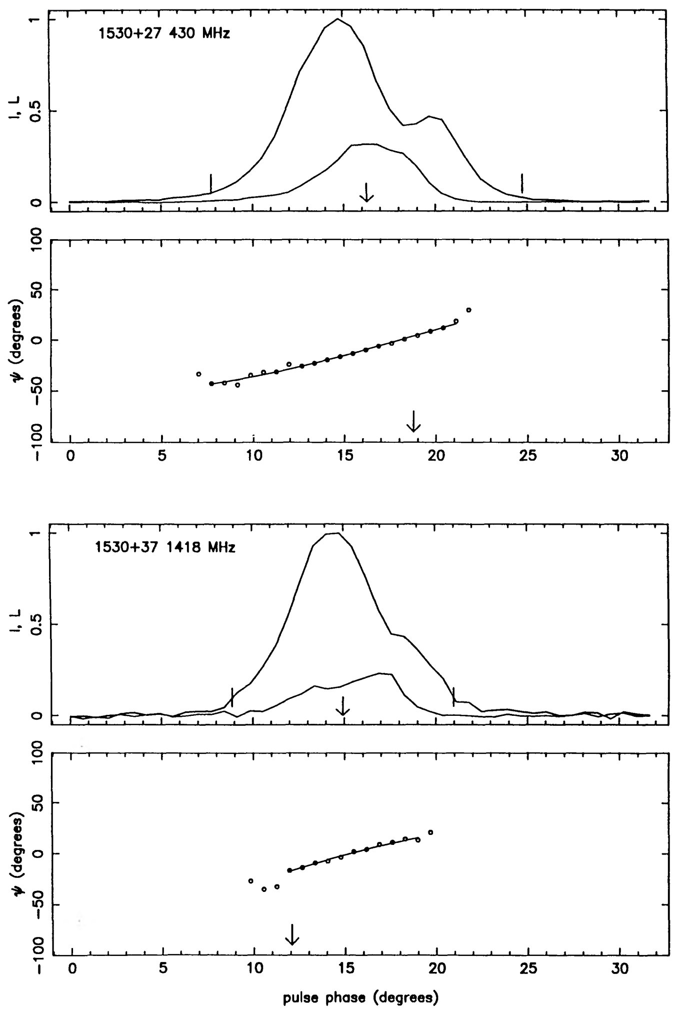

FIG. 13.—Total intensity, linearly polarized intensity, and position angle for 1530+27 at two frequencies. The pulse center marked by the arrow in the top panel is the pulse phase midway between the 5% intensity levels. The arrow on the position angle curve points to the maximum gradient in the fitted position angle curve.

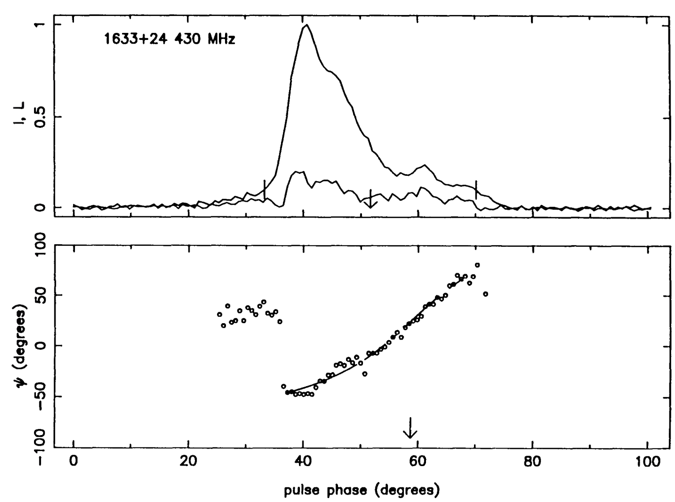

FIG. 14.—Total intensity, linearly polarized intensity, and position angle for 1633+24. The 10% intensity levels are indicated. The arrow on the position angle curve points to the maximum gradient in the fitted position angle curve.

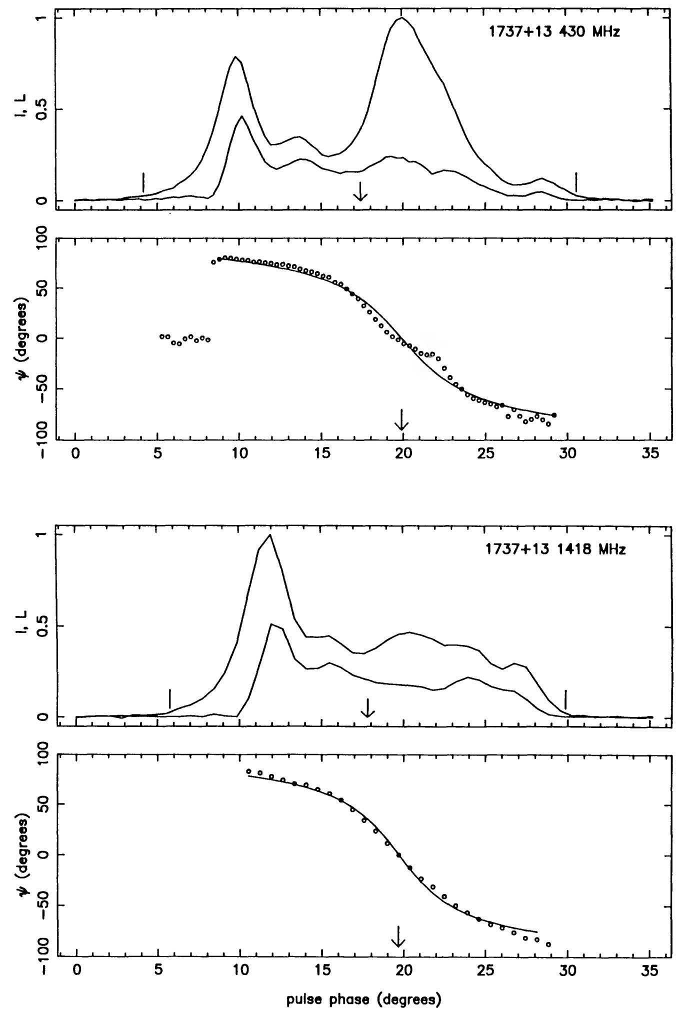

FIG. 15.—Total intensity, linearly polarized intensity, and position angle for 1737+13 at two frequencies. The pulse center marked by the arrow in the top panel is the pulse phase midway between the locations where the intensity rises above average. The arrow on the position angle curve points to the maximum gradients in the fitted position angle curve.

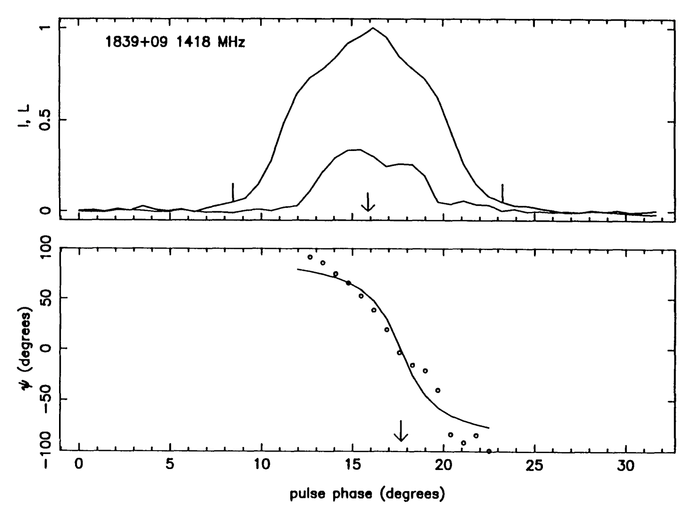

FIG. 16.—Total intensity, linearly polarized intensity, and position angle for 1839+09. The 5% intensity levels are indicated. The arrow on the position angle curve points to the maximum gradient in the fitted position angle curve.

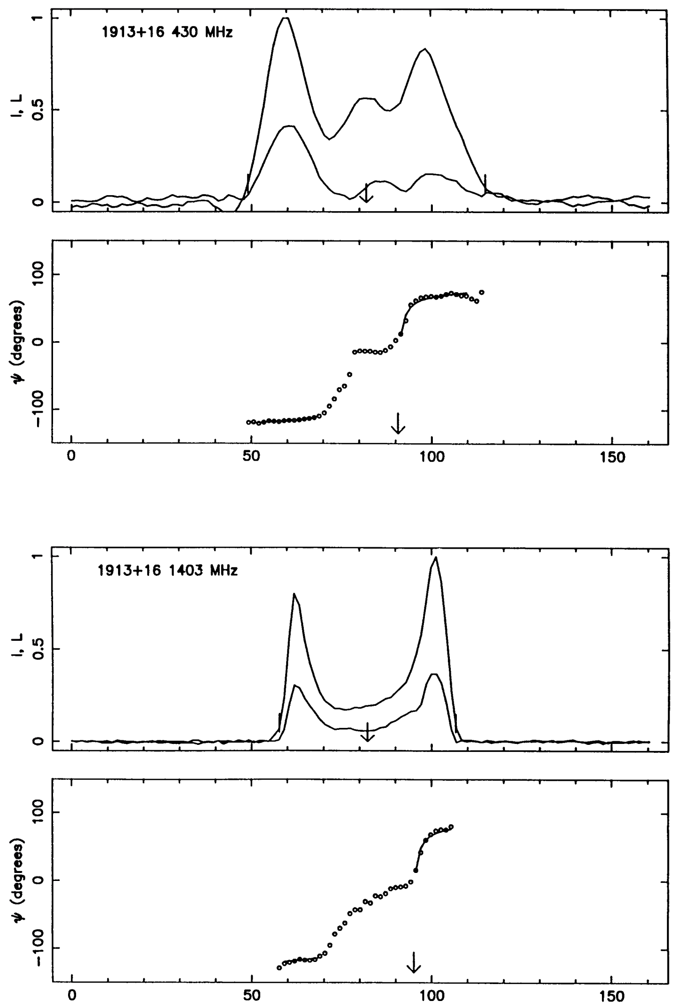

FIG. 17.—Total intensity, linearly polarized intensity, and position angle for 1913+16. The 10% intensity levels are indicated. The arrow on the position angle curve points to the maximum gradient in the fitted position angle curve.

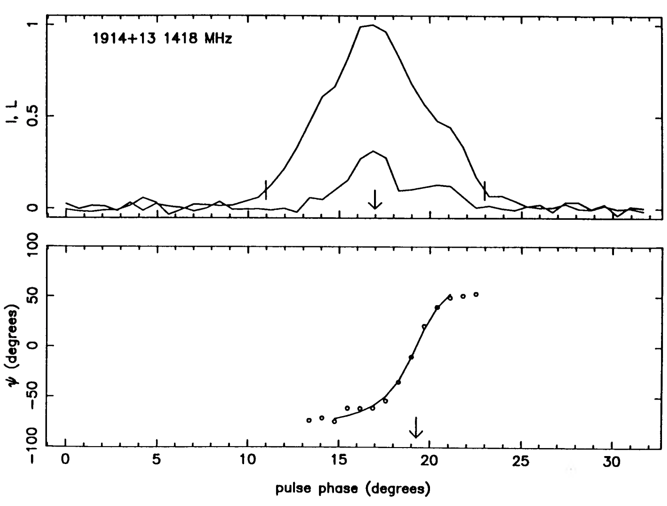

FIG. 18.—Total intensity, linearly polarized intensity, and position angle for 1914+13. The 10% intensity levels are indicated. The arrow on the position angle curve points to the maximum gradient in the fitted position angle curve.

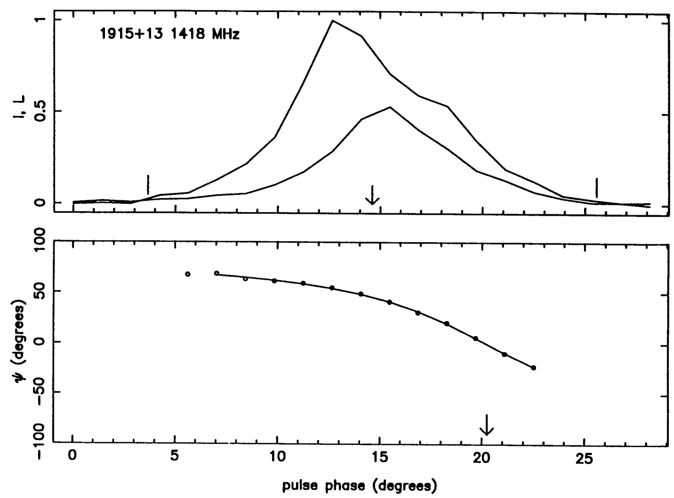

FIG. 19.—Total intensity, linearly polarized intensity, and position angle for 1915+13. The pulse phase midway between the locations where the intensity rises above average is indicated. The arrow on the position angle curve points to the maximum gradient in the fitted position angle curve.

with emission radii. The adopted value of r_{delay} was obtained assuming a phase lag $2^\circ \pm 2^\circ$ for both frequencies, which is consistent with most of the phase-lag estimates for both frequencies.

3.3.11. *1530+27*

R83 has tentatively classified 1530+27 as a conal double. The position angle curve of this pulsar is nearly linear, which is the reason for the large errors in the phase-lag estimates. The negative phase delays at 1.4 GHz are consistent with zero, as are the large phase lags at 0.43 GHz. Instead of ascribing different radii to the two frequencies, we calculated a single emission radius by weighting the phase lags according to their errors.

3.3.12. *1633+24*

The emission from this pulsar is of the conal type (R90). After excluding the obvious orthogonal moding at the leading edge of the pulse, the RVM fits the data well. The asymmetry of

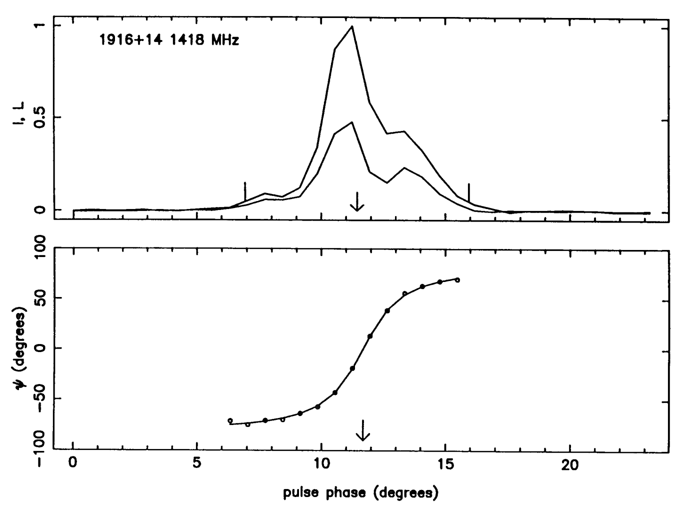

FIG. 20.—Total intensity, linearly polarized intensity, and position angle for 1916+14. The 5% intensity levels are indicated. The arrow on the position angle curve points to the maximum gradient in the fitted position angle curve.

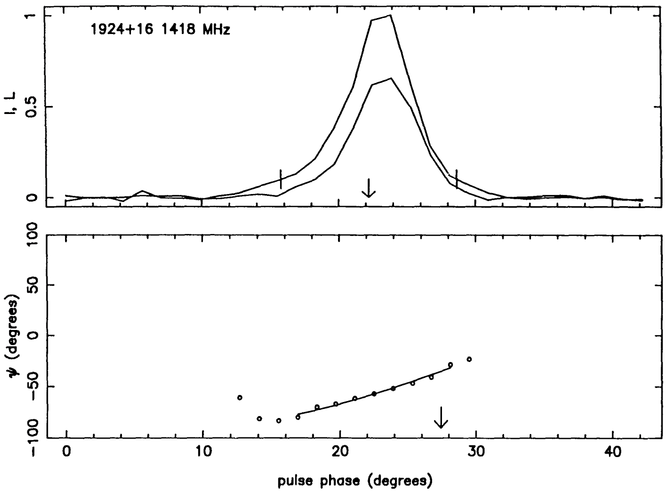

FIG. 21.—Total intensity, linearly polarized intensity, and position angle for 1924+16. The 10% intensity levels are indicated. The arrow on the position angle curve points to the maximum gradient in the fitted position angle curve.

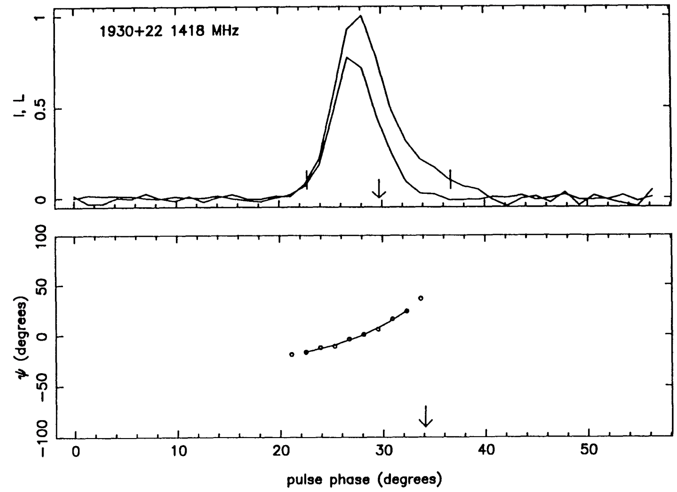

FIG. 23.—Total intensity, linearly polarized intensity, and position angle for 1930+22. The 10% intensity levels are indicated. The arrow on the position angle curve points to the maximum gradient in the fitted position angle curve.

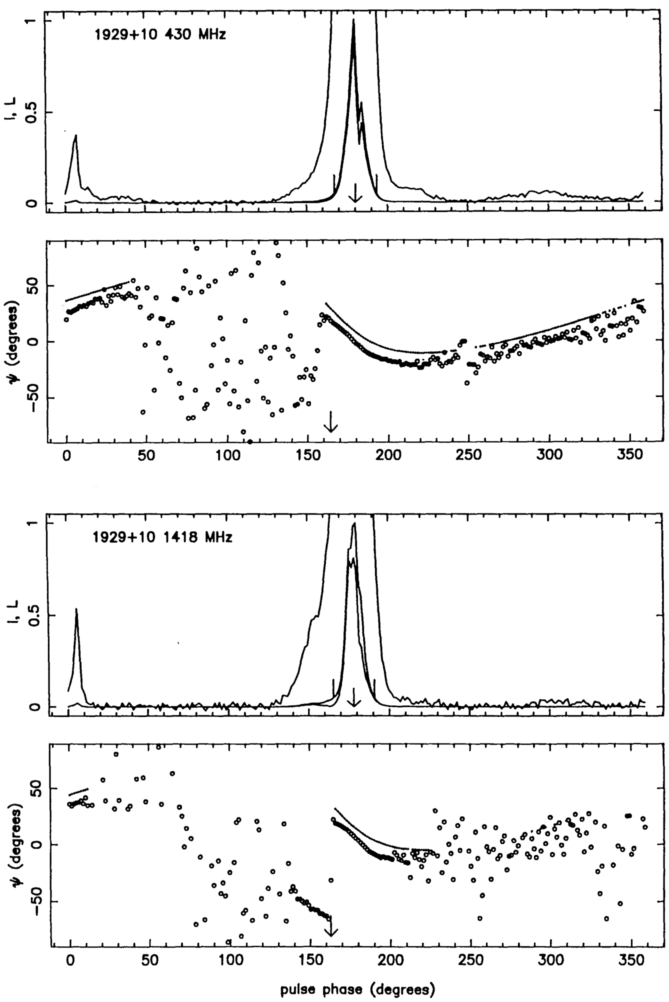

FIG. 22.—Total intensity, linearly polarized intensity, and position angle for 1929+10 at two frequencies. The pulse center marked by the arrow in the top panel is the pulse phase midway between the locations where the intensity rises above average. The total intensity multiplied by 25 is also plotted, so that the fine structure of the pulse shape is apparent. The arrow on the position angle curve points to the maximum gradient in the fitted position angle curve. The position angle fit has had 10° added to it for easy viewing.

the profile and the quality of the data caused us to use ϕ_1 to estimate the pulse center.

3.3.13. *1737+13*

The total intensity from this star exhibits two, statistically different, emission modes (Rankin, Wolszczan, & Stinebring 1988). Both modes have very similar position angle curves, so no attempt was made to separate the modes. Both the 0.43 and 1.4 GHz position angle curves are well approximated by the rotating vector model, but the different phase-lag estimates exhibit a lot of scatter. The nonuniformity is due to the asymmetry and strong frequency dependence of the intensity profile. The increase in component separation with wavelength suggests that the 1.4 GHz emission is emitted at a lower altitude than the 0.43 GHz emission, so $\Delta\phi_4$ was taken as the best estimate of the phase lag. The error on the emission radius was chosen so that most of the phase-lag estimates were consistent with the emission radius.

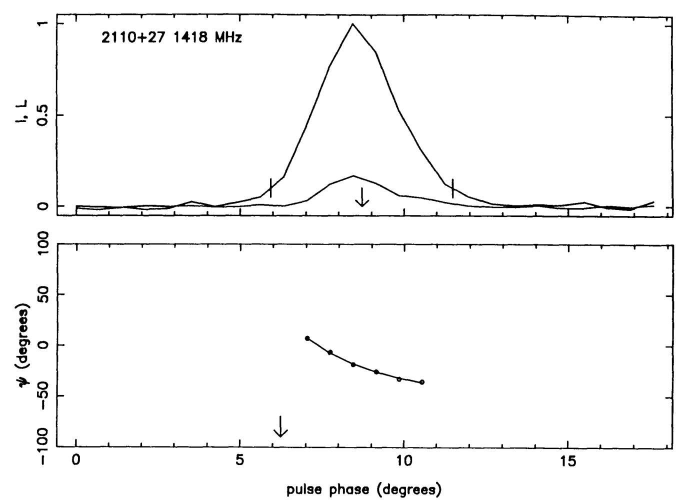

FIG. 24.—Total intensity, linearly polarized intensity, and position angle for 2110+27. The 10% intensity levels are indicated. The arrow on the position angle curve points to the maximum gradient in the fitted position angle curve.

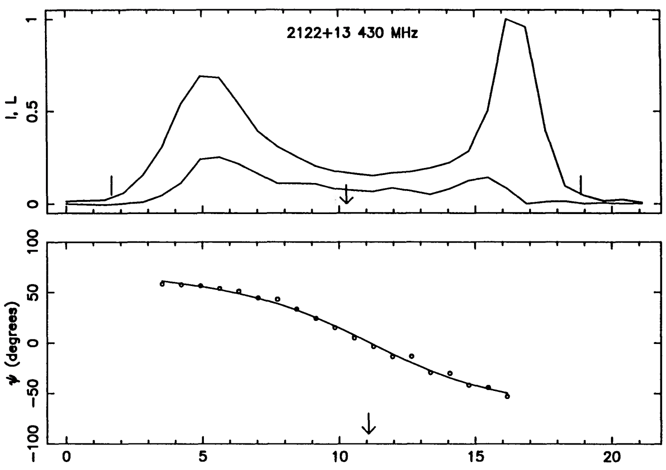

FIG. 25.—Total intensity, linearly polarized intensity, and position angle for 2122+13 at 430 MHz. The pulse center marked by the arrow in the top panel is the pulse phase midway between the 5% intensity levels. The arrow on the position angle curve points to the maximum gradient in the fitted position angle curve.

3.3.14. *1839+09*

Rankin identifies this object as a core single, and equation (17) does not fit the data very well, which is characteristic of core emission. Within measurement errors all the phase-lag estimates are the same, and r_{delay} was calculated assuming a phase lag of 2° ± 1°.

3.3.15. *1913+16*

This pulsar is in a binary system and may be undergoing geodetic precession (Bailes 1988; Weisberg, Romani, & Taylor 1989; Cordes, Wasserman, & Blaskiewicz 1990). As the 0.43 GHz profile suggests, 1913+16 has been categorized as a triple (R90).

From the figures it appears that the 10% width at 0.43 GHz is about 65°, whereas the value in Table 1 is 60°. The apparent discrepancy is due to the combined effects of interstellar scattering and interstellar dispersion. These propagation effects cause the 0.43 GHz profile to be convolved with a boxcar of full width 8°5 and with a one-sided exponential of equivalent width equal to 4°. In addition to the propagation broadening, the profile has been smoothed by 8° to increase signal-to-noise. We estimated the actual width by broadening the 1.4 GHz profile numerically, finding the increase in the 10% width due to the broadening, and subtracting the difference from the raw 10% width obtained from the 0.43 GHz waveform. The corrected width appears in Table 1. The values of α and β for the numerically broadened 1.4 GHz profile were the same as the values obtained from the unbroadened profile, so no corrections to the 0.43 GHz fitting parameters were made.

The central portion of the position angle curve has been excluded because of core emission in the center of the profile. As is clear from the figures, our estimates of ϕ_0 and the accompanying emission heights are strongly dependent on the region we used in fitting the curve. We justify our choice of fitting interval as follows.

The separation between the leading and trailing peaks in the intensity waveform is nearly the same at 0.43 and 1.4 GHz. The constancy of the peak separation with frequency argues that the radiation contributing to the peaks arises at roughly the same altitude for both frequencies. With our choice of fitting interval, aligning the waveforms using ϕ_0 aligns the peaks. If the fitting region is changed to include the initial rise of the position angle curve in the phase interval [70°, 80°] and exclude the tail end of the rise in the interval [95°, 98°], alignment of the waveforms using ϕ_0 misaligns the peaks by ~5°, with the 0.43 GHz profile leading the 1.4 GHz profile. Such a shift is expected if the 0.43 GHz emission originates at a larger radius than the 1.4 GHz emission. However, the radius-to-pulse-width mapping predicts that the peak separation at 0.43 GHz would be ~25% larger than the peak separation at 1.4 GHz if the 5° phase delay were present. The difference in peak separation is clearly less than 25%. In addition, the delay-radius relation yields negative emission radii for the second choice of fitting interval, which is at odds with most of the other data.

As stated in the previous paragraph, we believe that the radiation contributing to the leading and trailing peaks originates at roughly the same altitude for both frequencies. As a result, the estimates of r_{delay} were obtained by taking the centroid of the intensity waveform to be midway between the leading and trailing peaks and averaging the phase delays for both frequencies. The phase delay is 12°5 ± 1°, corresponding to an emission height of 156 ± 21 km for the radiation contributing to the leading and trailing peaks of the waveforms.

The core component of the 0.43 GHz waveform arrives at a later phase than the pulse center. Using the total intensity waveform, the 0.43 GHz core emission originates ~10 km below the cone emission. Using the linearly polarized intensity, the core emission originates ~40 km below the cone emission. Both of these results are consistent with the core emission originating at around 10 stellar radii.

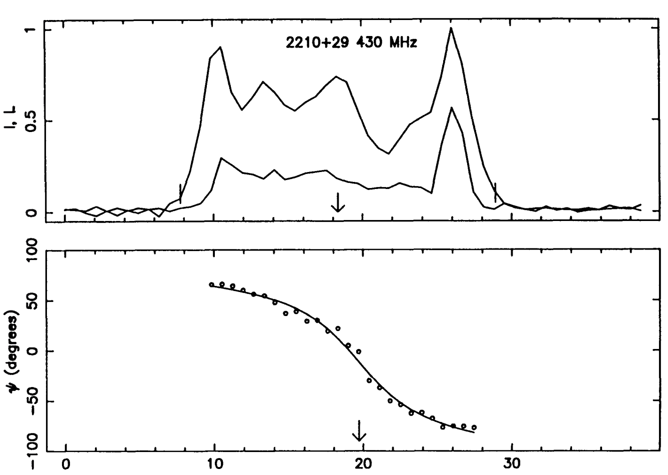

FIG. 26.—Total intensity, linearly polarized intensity, and position angle for 2210+29 at 430 MHz. The pulse center marked by the arrow in the top panel is the pulse phase midway between the 10% intensity levels. The arrow on the position angle curve points to the maximum gradient in the fitted position angle curve.

3.3.16. *1914+13*

This object has been classified as a core single (R90). Given the size of the statistical errors, equation (17) fits the position angle curve of the object extremely well, which is unusual for core emission. All the phase-delay estimates agree within measurement errors and r_{delay} was calculated assuming a delay of 2°4 ± 0°5.

3.3.17. *1915+13*

This object has been classified as a core single (R90). The intensity profile suggests at least two components. Equation (17) fits the position angle curve of this star very well. All the phase-lag estimates are the same within measurement errors, and $r_{\rm delay}$ was calculated assuming a phase lag of $6° \pm 2°$.

3.3.18. *1916+14*

The position angle curve of this triple star (R80) is well modeled by equation (17). Given the signal-to-noise and the asymmetry of the intensity profile, ϕ_1 was chosen as the best estimate of the pulse center.

3.3.19. *1924+16*

R90 classifies this object as a core single. The position angle curve is nearly linear, and all the phase-delay estimates are the same within measurement errors. The emission height was calculated assuming a phase delay of $5° \pm 3°$.

3.3.20. *1929+10*

This multicomponent profile shows evidence of core and cone emission as well as an interpulse. Equation (17) was fitted to the pulse in two different ways. In the first case the phase interval which includes the interpulse and the main pulse was fitted. The results of these fits are shown in Figure 22 and Table 2. Our fit parameter estimates are about midway between the estimates of LM88 and Phillips (1990). For the 1.4 GHz data the phase interval which includes the interpulse and the region of orthogonal moding before the main pulse was also fitted. The alternative fit parameters are also shown in Table 2. Given the fraction of pulse phase over which this second fit is valid, we do not consider the second fit as indicative of the emission geometry.

Even though equation (17) models the data over a large fraction of pulse phase, the magnetic field in the emission region appears to have nondipolar components. To justify this point of view, we note that both the 0.43 and the 1.4 GHz position angle curves for $1929+10$ have inflection points in the center of the main pulse, whereas neither of the fitted position angle curves has this property. The inflection points in the position angle curve suggest that nondipolar components of the magnetic field are present in the emission region. Since higher multipole moments decay more quickly with radius than the dipole component, the higher order moments become more important as the radius decreases, If we take the geometric emission radii as indicators of the true emission radius, then the emission occurs at about 50 stellar radii. The corrections to $\boldsymbol{b}$ due to nondipolar components would be 50 times larger at the stellar surface than in the emission region. The resulting distortion of the current flow could be quite substantial and lead to an asymmetric pulse shape. An asymmetric pulse shape could lead to the negative phase lags which this object exhibits.

The possibility that $1929+10$ has an asymmetric beam is further reinforced by the fact that there appear to be three nonoverlapping pulse components: the centroid of the third component is at $\sim 300°$. For all three components to be produced by a nearly symmetric beam requires aberration effects and time delays that we consider improbable. As a result we attribute the negative phase lags to an asymmetric pulse.

3.3.21. *1930+22*

This object has been classified as a core single by R90. All the phase-delay estimates are the same within measurement errors, and $r_{\rm delay}$ was calculated assuming a delay of $5° \pm 5°$.

3.3.22. *2110+27*

This pulsar has been classified as a conal single in R90. Given the noise level, equation (17) fits the ψ-curve of this pulsar extremely well, which is something of an embarrassment given that all the phase-lag estimates are negative. However, since the phase interval used to fit equation (17) is quite short, a parabola would fit the data as well as equation (17). Thus, the small fit residuals *do not* indicate that the magnetic field in the emission region is dipolar.

The upper limit of the emission height using the radius–to–pulse-width mapping is 95 km, which is fairly small when compared with other objects that have predominantly conal emission. If only half the beam is present, the geometric emission radius would be underestimated by a factor ~ 4. If this is the case, the actual emission height is ~ 400 km, which is in agreement with the other pulsars that exhibit predominantly conal emission. Perhaps nondipolar fields or an asymmetric emission region are present, as with $1929+10$.

3.3.23. *2122+13*

This conal double profile was observed only at 0.43 GHz. The asymmetry of the profile, and the fairly low signal-to-noise ratio, suggest that the pulse edges are best defined using the 5% or 10% intensity level. The phase lag $\Delta\phi_1$ did not change significantly between these levels, and was used in the delay-radius relation to obtain the emission radius estimate.

3.3.24. *2210+29*

Good polarimetry of this five-component profile was obtained only at 0.43 GHz. The asymmetry of the profile, and the low signal-to-noise, require us to treat this object like $2122+13$. As with $2122+13$, the sharp edges of $2210+29$'s profile made estimates of pulse center using 5% and 10% levels nearly identical. The emission radius, and its quoted error, used the 10% level.

3.4. *Generalizations*

As a whole, equation (17) models the data extremely well. For the data we have fitted, the rms values of the fit residuals are usually within a factor of 2 of the expected rms assuming purely statistical fluctuations.

Of the 23 pulsars for which we have data, 12 exhibit position angle curves that are S-shaped ($0301+19$, $0525+21$, $0751+32$, $0950+08$, $1133+16$, $1737+13$, $1913+16$, $1914+13$, $1916+14$, $1929+10$, $2122+13$, $2210+29$). These objects will be denoted as group A. Of the group A objects, six have positive $r_{\rm delay}$ at the 90% confidence level, and one ($1929+10$) has a negative $r_{\rm delay}$ at the same level of confidence. Consider only the seven objects which have the sign of $r_{\rm delay}$ accurate at the 90% confidence level. Given equal probabilities for negative and positive delays, calculation using the binomial distribution gives a 6% chance that at least six of the seven delays are positive.

After removal of the group A objects, eight of the remaining objects ($0540+23$, $0611+23$, $1530+27$, $1633+24$, $1915+13$, $1924+16$, $1930+22$, $2110+27$) exhibit position angle curves that appear to be the leading or trailing half of an S-shaped curve. These are the group B objects. Five of the group B objects have nonzero values of $r_{\rm delay}$ at the 90% confidence level, and four are positive at this level of confidence. Given equal probabilities for negative and positive delays, there is a 20% chance that at least four of the five delays are positive.

After removal of groups A and B, only three objects remain ($0823+26$, $0919+06$, $1839+09$). These group C pulsars have position angle curves that appear to be contaminated by a substantial amount of unresolved, orthogonal moding. Of the group C objects, two have positive values of $r_{\rm delay}$ at the 90% confidence level, and the last is unconstrained at this level of confidence. Given equal probabilities for negative and positive delays, there is a 25% chance that both of the constrained delays are positive. When all three groups are considered, and if the probability of negative and positive delays is the same, the probability of at least 12 positive delays out of 14 is 1%.

Another way of testing the probability that our procedure measures emission radii is to employ a Kolmogorov-Smirnov test of the cumulative distribution function. We have a total of 35 estimates of $\Delta\phi_1$. Conservatively, from our fits, we cannot exclude the possibility that as many as nine of these values are negative. If we assume that our data are a fluke that arose from a population that had an equal probability of positive and negative $\Delta\phi_1$, then the true cumulative distribution at $\Delta\phi_1 = 0$ would be 0.5. A rough upper bound on the cumulative distribution function at $\Delta\phi_1 = 0$ for our data may be derived by assuming the actual values of $\Delta\phi_1$ to be $\Delta\phi_1 - \sigma(\Delta\phi_1)$, i.e., by lowering the best-fit $\Delta\phi_1$ values by their 1 σ uncertainties. This procedure indicates that the cumulative distribution function at $\Delta\phi_1$ is probably less than 0.26. Using the asympotic expression for the Kolmogorov-Smirnov test (see, e.g., Lindgren 1962), the probability that our data arose from a population with equal probabilities of negative and positive $\Delta\phi$ is $\lesssim 2\%$. It appears that our results are not statistical fluctuations.

With 1 σ certainty, 0301+19, 0525+21, 0540+23, 0751+32, 0823+26, 1133+16, and 1929+10 have radio emission originating on field lines that bend away from the spin axis. To the same degree of certainty, only 0950+08 and 1913+16 have radio emission originating on field lines that bend toward the spin axis. The tendency for emission to occur on field lines that bend away from the spin axis was previously observed by Narayan & Vivekanand (1982, hereafter NV82), who fitted polarization data in a manner similar to ours.

Unlike NV82, we find no tendency for alignment of the spin and magnetic axes. Within the error bars, four objects have $\alpha > 90°$, and four objects have $\alpha < 90°$. Using the 11 objects which have errors in α of less than 60°, $\overline{\sin\alpha} = 0.75 \pm 0.09$ and $\sigma(\sin\alpha) = 0.29 \pm 0.12$. For a random orientation between the spin and magnetic axes, $\overline{\sin\alpha} = 0.78$ and $\sigma(\sin\alpha) = 0.22$. Our data are consistent with a random distribution between the orientation of the spin and magnetic axis.

3.5. *Implications for Waveform Classification*

Many high-quality polarization profiles may be found in the literature. Unfortunately, most of the phase lags, positive or negative, are too small to be measured by eye. The only exceptions to this rule that we are aware of are the members of the "one-sided conal class" introduced in LM88. Five of the pulsars in our study (0540+23, 0919+06, 1530+27, 1915+13, and 1924+16) have been classified as one-sided cones (LM88). A principal reason for their classification is that their polarization curves lag their intensity profiles by a significant fraction of the pulse width.

Figure 27 shows the intensity profiles of 0540+23 and 0919+06 aligned using the center of the position angle curve. For both cases the 0.43 GHz profile leads the 1.4 GHz profile by a substantial fraction of the pulse width. If the 0.43 GHz emission originates at a higher altitude than the 1.4 GHz emission, the relativistic flow model predicts that the 0.43 GHz waveform should lead the 1.4 GHz waveform when the waveforms are lined up using ϕ_0. However, the relativistic flow model also predicts that the 0.43 GHz waveform should be wide enough that its leading and trailing edges lie outside the leading and trailing edges of the 1.4 GHz waveform; the increase in width should be larger than the increase in phase lag.

Prototypical examples of what the relativistic flow model predicts are shown in Figure 28. For 0301+19 and 0525+21 the 0.43 GHz waveform leads the 1.4 GHz waveform, and the edges of the 0.43 GHz profile lie outside the edges of the 1.4 GHz profile. Since the profiles of 0540+23 and 0919+06 do not have the second quality, we conclude that asymmetries are present in the beams of 0540 + 23 and 0919 + 06, and go on to consider each of these objects separately.

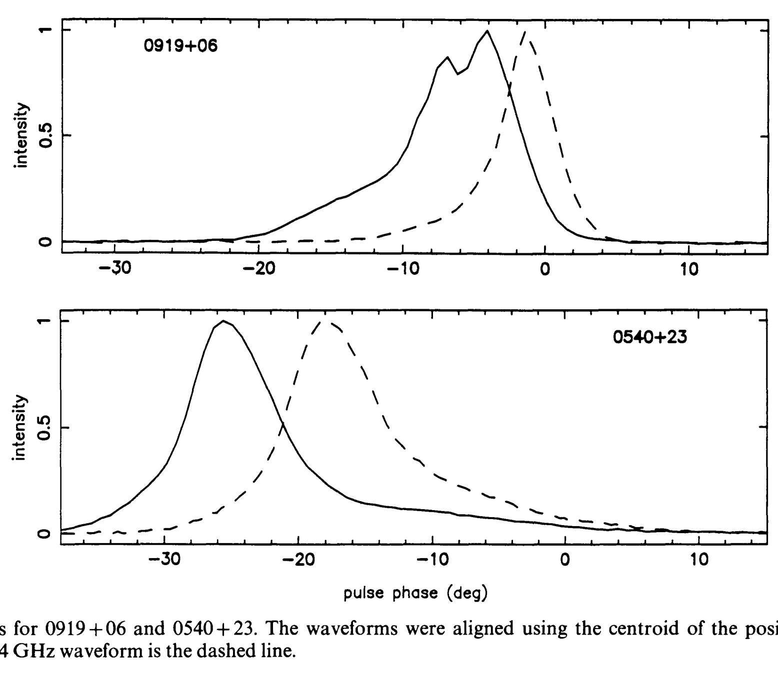

FIG. 27.—Total intensity profiles for 0919+06 and 0540+23. The waveforms were aligned using the centroid of the position angle curve ϕ_0. The 0.43 GHz waveform is the solid line, and the 1.4 GHz waveform is the dashed line.

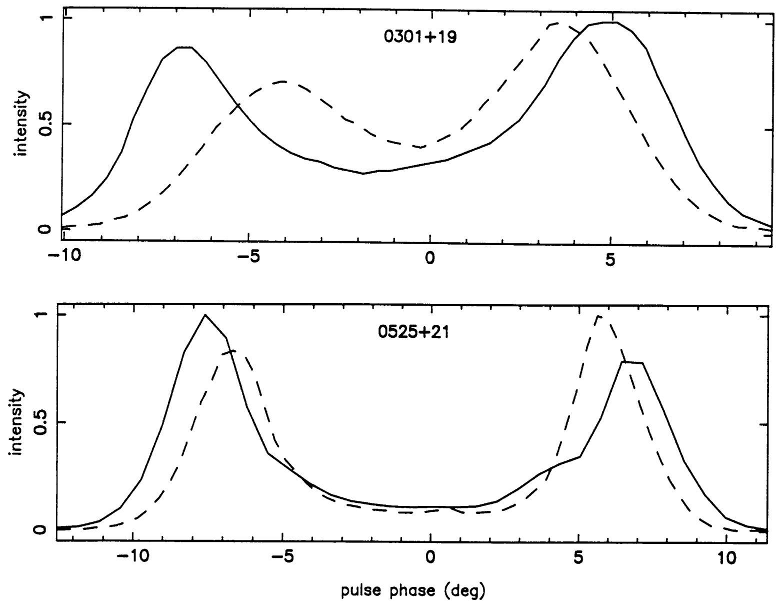

FIG. 28.—Total intensity profiles for 0301+19 and 0525+21. The waveforms were aligned using the centroid of the position angle curve ϕ_0. The 0.43 GHz waveform is the solid line, and the 1.4 GHz waveform is the dashed line.

In the case of 0919+06 a single component is visible at 1.4 GHz. At 0.43 GHz there appear to be two or even three components (R90), with the trailing component at 0.43 GHz corresponding to the component which is visible at 1.4 GHz. Since core components tend to persist with frequency, we take the component visible at 1.4 GHz to be a core component. If this interpretation is correct, then the emission height at 0.43 GHz listed in Table 3 is overestimated, since the pulse center at this frequency was obtained by taking the point midway between the pulse edges. The true pulse center at 0.43 GHz would be located at the peak of the core component, so the true emission height at 0.43 GHz would be closer to the emission height at 1.4 GHz.

In the case of 0540+23 it appears that we see only the leading edge of a conal double profile. Assume that the leading edge of the pulse corresponds to emission at the boundary of the open field line region, and that the delay-radius relation is satisfied. Let $\Delta\phi_L$ denote $\phi_0 - \phi_L$, where ϕ_L is the phase at the leading edge of the pulse. By combining equation (19) with the delay-radius relation, we find that the emission height will be constrained by

$$\Delta\phi_L = \frac{1}{\sin\alpha}\left(\frac{9\Omega r}{4} - \sigma^2\right)^{1/2} + 4\Omega r \,.$$

Setting ϕ_L equal to the phase at the 10% intensity level on the leading edge of the pulse gives emission radii of 720 and 550 km for the 0.43 and 1.4 GHz emission, respectively.

LM88 note that the fraction of leading one-sided cones (72%) is nearly the same as the fraction of conal doubles in which the leading components is stronger that the trailing component. They ascribe the one-sided cones to extreme members of the conal double class. It may be that the generally observed asymmetry is due to the sort of effects apparent in Figure 3, while the one-sided profiles are due to a different effect.

Within the context of the coherent curvature model of § 2.4, the average, observed intensity as a function of pulse phase could be modeled as $I(\phi) = I_0(\phi)n(\phi)$, where $I_0(\phi)$ would be the observed intensity for a plasma distribution with $n = H(1 - \delta^2/\Omega r_{em})$, and $n(\phi)$ is the time-average distribution in the corotating frame of a particular pulsar. Let $\phi = 0$ correspond to the pulse phase midway between the leading and trailing edges of the pulse. Suppose that the probability distribution, over the pulsar population, of $n(\phi)$ is symmetric in ϕ. Then the observed distribution of peak ratios would be obtained if $I_0(\phi)$ is asymmetric in ϕ and if the fluctuations in $n(\phi)$ were of the appropriate magnitude. The chance that part of the beam would completely disappear would depend on extreme values of $n(\phi)$ and would be essentially independent of any general trends in pulse shape. The observed distribution would also depend on the absolute brightness of the pulse. For the parameters used in Figure 8, the difference in peak brightness is of order 25%, which we take to be a fiducial value. For a flux-limited search, with everything else being equal, a leading cone that was just detectable at 1 kpc would be just detectable at $(0.75)^{1/2}$ kpc if it were a trailing cone. Assuming a uniform two-dimensional distribution of pulsars (they lie nearly in the Galactic plane) ~57% of the one-sided cones detected would be leading cones. In this case the observed fraction of leading one-sided cones would be closer to 0.5 than is observed. We go on to explore this possibility.

Using Table 1 in LM88, 36% of their conal double profiles have pulse periods of less than 0.5 s. Table 4 of LM88 indicates that 18 of the 32 one-sided cones have periods less than 0.5 s. Additionally, the fast pulsars in the one-sided cone list tend to have polarization curves which lag their intensity profiles. It seems reasonable to suppose that some of the objects LM88 classify as one-sided leading cones are, in fact, produced by a symmetric emission region and that their classification as one-sided cones is due to the lag predicted by the delay-radius relation. The five fastest pulsars in Table 4 of LM88 are all leading cones, have an average period ~0.17 s, and have an average pulse width of 20°. Assuming that the position angle curve is centered at the trailing edge of the intensity profile gives $r_{delay} \sim 350$ km, which is in qualitative agreement with most of the emission radii shown in Table 3 of our paper.

3.6. *Relationship of Emission Radius to Other Parameters*

The values of r_{delay} obtained in § 3.3 depend on the position angle curve near the center of the pulse and on the intensity in the pulse wings. Therefore, the values of r_{delay} are averaged over all emitting regions. The values of r_{geo} (cf. eq. [19] and Table 3) are most sensitive to the intensity in the pulse wings, and provide estimates of the emission radius at the pulse edges. When distinct core and cone components are present, r_{geo} will be dominated by the cone components, and r_{delay} will be an average over all components.

Seven of the pulsars (0301+19, 0525+21, 0751+32, 1133+16, 1737+13, 1913+16, 2122+13, and 2210+29) have well-spaced, reasonably symmetric conal outriders with an extended bridge of emission or distinct central emission components. All these objects are consistent with $r_{delay} \leq r_{geo}$, and three of the seven require inequality for the emission radius estimates to be within 1 standard deviation. None of the other pulsars require $r_{delay} < r_{geo}$ for their emission radius estimates to be accurate within 1 standard deviation, and most of them are consistent with $r_{delay} = r_{geo}$. Therefore, our data suggest that core emission originates slightly closer to the star than conal emission.

Eight of the pulsars (0549+23, 0611+22, 0823+26, 1839+09, 1914+13, 1915+13, 1924+16, and 1930+22) have been identified as core single stars. As a rule the core single profiles are narrower than the profiles with conal emission, and the geometric emission heights are marginally smaller for core single stars than for stars which have cone emission. We do not find any significant difference in r_{delay} between core and conal types, which suggest that the core emission process in similar in the two groups.

Given that r_{delay} does not have a significant dependence on morphological type, we examine the dependence of r_{delay} on observing frequency. For 11 objects we have estimates of r_{delay} at both frequencies. For three of these, r_{delay} at 0.43 GHz differs from r_{delay} at 1.4 GHz by more than 1 standard deviation, and all of these objects have larger r_{delay} at 0.43 GHz than at 1.4 GHz. The uncertainties preclude quantitative estimates, but our data are consistent with, if not suggestive of, emission radius increasing with wavelength. When the entire data set is weighted uniformly, the 0.43 GHz data give $\bar{r}_{delay} = 440$ km and $\sigma(r_{delay}) = 270$ km. For uniform weighting of all 1.4 GHz data, $\bar{r}_{delay} = 310$ km and $\sigma(r_{delay}) = 200$ km. The difference between the averages is only 40% of the expected standard deviation of the difference, but the data are consistent with emission radius increasing with wavelength. The possibility of a radius-to-frequency mapping will be treated more fully in § 5.

Our results are consistent with altitudes determined from multifrequency timing observations (Cordes 1978; Matese & Whitmire 1980; Cordes & Stinebring 1984; Cordes et al. 1990; Phillips & Wolszczan 1990). Such observations demonstrate consistency of frequency-dependent arrival times with the cold plasma dispersion relation and thereby put limits on differential aberration and retardation resulting from a variation of emission radius with frequency. Upper limits on the radial extent of the emission region are 6 km for 1937+214 (Cordes & Stinebring 1984); 200 km for 0823+26, 0834+06, 0919+06, 0950+08, 1133+16, and 1604−00 (Phillips & Wolszczan 1990); and 600 km for 0525+21 (Cordes 1978).

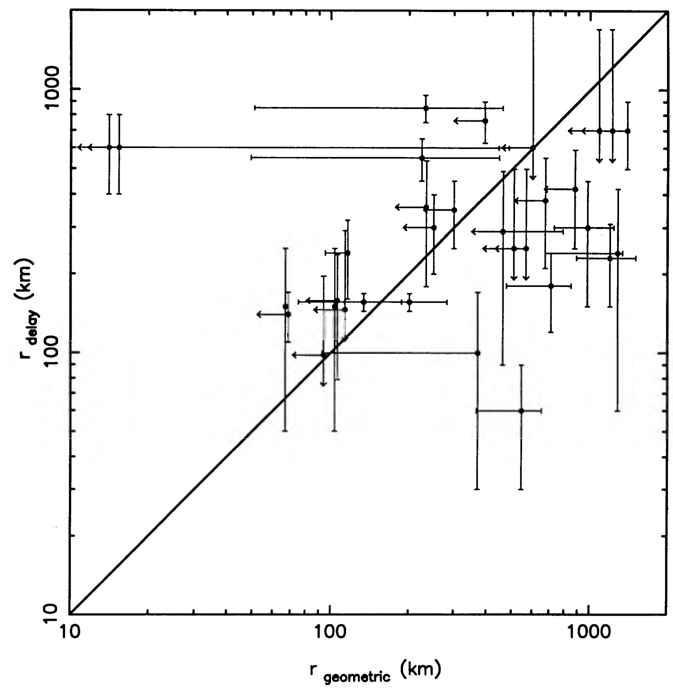

FIG. 29.—Scatter plot of emission height as measured using the delay-radius relation vs. emission height obtained using the radius–to–pulse-width mapping. Error bars are 1 standard deviation, and arrows indicate that the error bar leaves the frame of the graph.

Figure 29 shows a scatter plot of emission radius measured using the delay-radius relation r_{delay} versus the emission radius obtained using the radius–to–pulse-width mapping r_{geo}. We remind the reader that r_{geo} was calculated using the 10% width. Plotted on this same graph is $r_{delay} = r_{geo}$. For about 70% of the objects the emission radii obtained by the two methods are within 1 standard deviation of each other. A few of the points lie well away from the line. Within the context of the relativistic flow model, (1) the emission radius in the center of the pulse could be quite different from the emission radius at the edge of the pulse, (2) our estimate of the phase at which δ is a minimum could be off, and (3) the 10% width may underestimate the correct value of the flux-tube width.

Given the uncertainties, no rigorous statements are possible, but the fact that all the orders of magnitude jibe does make it seem likely that the open field line region satisfies $\delta^2 \leq \Omega r$. This is consistent with the assumptions made in § 2 and supports the validity of equation (18).

4. COMPARISON WITH OTHER INTERPRETATIONS OF PULSAR POLARIZATION

In a set of papers, Ferguson (1973, 1976) proposed and extended a polarization model which supposes that the emission region is essentially a point source that corotates with the neutron star. The point source emits polarized radiation which is characterized by a single vector. This vector behaves like a solid bar under Lorentz transformations, and is physically identified with a magnetic field line. The position angle of the radiation is taken to be the apparent position angle of the bar on the plane of the sky, and the degree of linear polarization is taken to the proportional to the apparent length of the bar. Relativistic effects are due to Lorentz contraction of the bar along the direction of the corotation velocity, and to a time delay resulting from finite propagation speed. For emission within the region bounded by equation (18), both of these effects are second order in Ωr. Given that radio emission is thought to be from relativistic plasma, and probably occurs well within the light cylinder, the first-order effects derived in this paper will dominate the effects calculated by Ferguson. Additionally, the effects calculated by Ferguson depend on the magnetic field geometry near the light cylinder, which is unknown.

Shitov (S85) considers the effects of a radiation term in the large-scale fields. The procedure amounts to adding a wave field, $\boldsymbol{B}_{\rm wave}$, to the dipole field, $\boldsymbol{B}_0$, where

$$\boldsymbol{B}_{\rm wave} = \frac{f\Omega^2}{3}\, \boldsymbol{m} \times \boldsymbol{\Omega} \, . \tag{23}$$

Assuming a corotation electric field outside the star, one may show that equation (23) is the leading term in a vacuum solution of Maxwell's equation. When the wave term is added to the dipole field, the system has a net Poynting flux; setting $f = 1$ gives an energy loss rate equal to that for magnetic dipole radiation. The wave term causes field lines to sweep back, which in turn causes the open field line region to be asymmetric with respect to the magnetic azimuth. In Shitov's analysis the radiation term causes the open field line region to be shifted in phase by an amount $\sim(\Omega r)^3$. He finds that the asymmetry causes the intensity profile to lag the polarization curve by an angle $\sim(\Omega r)^3$. For emission well within the light cylinder, the phase delay predicted by us should greatly dominate the effect predicted by Shitov.

In addition to his theoretical analysis, Shitov presents some measured values of the phase lag from pulsar radio data. He identifies the center of the intensity profile with the phase midway between the half-peak intensity levels. Pulse centers found using the half-intensity levels can be very different from pulse centers found using our methods. Given that the pulse components are often located asymmetrically within the total beam (LM88), we believe our first and fourth methods have better physical motivation than Shitov's method. In Shitov's analysis the center of the position angle curve was identified with the maximum gradient of the position angle data. The statistical errors inherent in his method of evaluating ϕ_0 are much larger than the random errors associated with fitting the RVM equation. In addition, Shitov's approach does not allow a quantitative measure of how well the RVM explains the data. For these reasons we believe that Shitov's results may not reflect the true conditions in the emission region.

A polarization model, based on propagation effects, has been put forth by Barnard (B86). In his model, radiation is generated near the star, and the emission direction is taken to be along the magnetic field. The radiation propagates away from the star until it reaches a polarization-limiting region, which may lie at a substantial fraction of $R_{\rm lc}$. In the polarization limiting region the radiation normal modes are assumed to be tightly coupled, with the end result being that the polarization vector is along, or orthogonal to, the projection of the local magnetic field on the plane of the sky. The radiation is then taken as incident on the interstellar medium, through which it propagates to the observer.

Figure 1 of B86 appears to show an offset between the center of the position angle curve and the δ-curve. For polarization fixed inside the light cylinder, the offset appears to be in the opposite direction from the offset predicted by the relativistic flow model, which is in conflict with our data.

5. ON THE PERIOD–PULSE-WIDTH RELATION AND THE RADIUS-TO-FREQUENCY MAPPING

5.1. *The Period–Pulse-Width Relation*

Consideration of Figure 29 shows that the geometric emission heights and the emission heights obtained using the delay-radius relation range over a couple of orders of magnitude and are concentrated in the vicinity of 300 km. Given the possibility of systematic errors, our results are consistent with tightly beamed emission from relativistic plasma which fills the open field line region, a radius–to–pulse-width mapping. This result is in conflict with the emission height of 10 km for core single stars, advocated by Rankin (R90). In the rest of this section we review Rankin's data, and present an emission model which accounts for those data within the context of a radius–to–pulse-width mapping.

Rankin (R90) has obtained a very interesting inequality. R90 finds that the 50% pulse widths (in *radians*) of core single stars, for an observing frequency of 1 GHz, satisfy $W_{50} \geq 3(\Omega R_*)^{1/2}$, with $R_* = 9.7$ km. All of the 50 core single stars studied in R90 satisfy the pulse-width–period inequality, and six have widths and periods that lie on the boundary of the inequality within very tight error bars. Quite plausibly, R90 suggests that core emission originates at a radius ~ 10 km. This result is clearly at odds with our results, and, given the large disparity between R90's emission height and ours, appears to rule out a radius–to–pulse-width mapping. In fact, for beamed emission from $r = R_*$ equation (19) gives $W_{50} \leq (9\Omega R_* - 4\sigma^2)^{1/2}/\sin\alpha$. As Rankin points out, there is probably some mechanism present to keep pulse widths from becoming narrow for large values of σ. This section is concerned with presenting a mechanism of this sort.

To model the emission process, we ignore the effects of aberration and retardation. To lowest order, assume that the emission per unit volume per unit solid angle is given by

$$J(\boldsymbol{r}, \ell) = \delta[\hat{\ell} - \boldsymbol{b}(\boldsymbol{r})]F(r)H\left(1 - \frac{\delta^2}{\Omega r}\right) . \tag{24}$$

In equation (24) $\hat{\ell}$ denotes a unit vector, and the delta function is over emission directions. The emission fills the open field line region and is beamed along the magnetic field, and its magnitude $F(r)$ is a function of radius only. To get the observed pulse shape the emission per unit volume needs to be integrated over the region of space which beams into our telescope. With the assumptions above, the observed power will be a function of δ alone:

$$P(\delta) = \int d^3r\, d^2\hat{\ell}\, J(\boldsymbol{r}, \hat{\ell})H\left(1 - \frac{|\hat{\ell} - \hat{\boldsymbol{n}}|}{\Delta\Sigma}\right) . \tag{25}$$

In equation (25) $\Delta\Sigma$ is the solid angle subtended by the telescope as measured at the neutron star. The integral over $\hat{\ell}$ is trivial, owing to the delta function, with the result that

$$P(\delta) = \int d^3r\, F(r)H\left(1 - \frac{\delta^2}{\Omega r}\right)H\left(1 - \frac{|\boldsymbol{b}(\boldsymbol{r}) - \hat{\boldsymbol{n}}|}{\Delta\Sigma}\right) . \tag{26}$$

The open field line region is given by $\delta^2 \leq \Omega r$, so, for a given δ, the minimum radius at which the integrand is nonzero is given by $r_{\rm min} = \delta^2/\Omega$. The Heaviside function with the dependence on $|\boldsymbol{b} - \hat{\boldsymbol{n}}|$ will act like an angular delta function for any reasonable set of parameters. We assume that the emission per unit volume peaks at a radius r_e and decays on a length scale R_0.

The pulse shape is given by

$$P(\delta) = K \int_{\delta^2/\Omega}^{\infty} r^2 F\left(\frac{r - r_e}{R_0}\right) dr$$
$$= G\left(\frac{\delta^2}{\Omega R_0} - \frac{r_e}{R_0}\right) . \quad (27)$$

In equation (27) K is a constant that depends on the size of the telescope and other parameters. In the limit that $R_0 \ll r_e$, $G \approx K r_e^2 \int F\, dr$. For $R_0 \gtrsim r_e$ the relationship between G and F becomes a little more complicated, but this has no effect on the rest of the argument.

Since profiles are observed as a function of pulse phase ϕ, the observed pulse profile is given by

$$P(\phi) = G\left[\frac{\delta^2(\phi)}{\Omega R_0} - \frac{r_e}{R_0}\right]$$
$$= G\left[\frac{4}{9\Omega R_0}(\sigma^2 + \phi^2 \sin^2 \alpha) - \frac{r_e}{R_0}\right] . \quad (28)$$

In equation (28) a natural scale for ϕ is $(\Omega R_0)^{1/2}/\sin \alpha$. For fixed G, R_0, and r_e this suggests a relationship between period and pulse width. As an example, take $G(x) = \exp(-x)$, where

$$x = \frac{4}{9\Omega R_0}(\sigma^2 + \phi^2 \sin^2 \alpha) - \frac{r_e}{R_0} .$$

The observed pulse shape is a Gaussian, with $W_{50} = 2.5(\Omega R_0)^{1/2}/\sin \alpha$: setting $R_0 = 14$ km gives the inequality found by Rankin. Additional forms of $G(x)$ which satisfy the pulse-width–period inequality are given by

$$G(x) = \begin{cases} \min[1, \exp(-x)] , & R_0 = 14 \text{ km} , \\ 1 - \tanh(x) , & R_0 = 28 \text{ km} . \end{cases}$$

In the first case, the emission per unit volume vanishes below r_e, while in the second case the emission per unit volume peaks near r_e and drops off smoothly on either side of the peak. In both cases the lower bound on the observed pulse width is determined by R_0, but the radius of peak emission is determined by r_e.

We do not suggest that the actual emission scenario is as simple as the one we present. Equation (24) was assumed to make simple, analytic statements possible. Additionally, the actual angles involved in pulsar beaming can be quite large, so the small-angle approximations we have invoked may be inaccurate. We only wish to show that Rankin's observations may be explained within the context of relativistic beaming if the emission per unit volume *changes* on length scales of the order of the stellar radius. The actual radius at which emission occurs can be much larger. As a result, Rankin's work is not at odds with a radius–to–pulse-width mapping or the emission radii presented by us.

5.2. *The Radius-to-Frequency Mapping*

Inspection of Table 3 shows that all the estimates of $r_{\rm delay}$ are consistent with

$$\frac{r_{\rm delay}(0.43\ \text{GHz})}{r_{\rm delay}(1.4\ \text{GHz})} \equiv f_{\rm delay} \geq 1 .$$

For all objects, except 0611 + 22, the geometric emission height estimates suggest

$$\frac{r_{\rm geo}(0.43\ \text{GHz})}{r_{\rm geo}(1.4\ \text{GHz})} \equiv f_{\rm geo} \geq 1 .$$

The uncertainties associated with the inequalities are quite large, but we consider the general trend to be important enough for independent discussion.

Assuming a dipolar magnetic field and relativistic plasma flow, the plasma density above the pair-creation zone will decrease as r^{-3}. A natural lower bound on the emission radius is the radius at which the plasma frequency ω_p and wave frequency ω are equal in the rest frame of the plasma. At this radius the wave in the rest frame of the plasma is essentially electrostatic (CR79) with the relationship between the plasma and wave frequencies in our frame given by

$$\omega^2 = \gamma \omega_p^2 . \quad (29)$$

In equation (29) ω is the radiation frequency in our frame, ω_p is the plasma frequency in our frame, and γ is the Lorentz factor of the (assumed monoenergetic) plasma. If the Lorentz factor does not change with radius, then the minimum emission radius as a function of frequency is given by $r_{\rm min}(\nu) \propto \nu^{-2/3}$. This plasma frequency scaling gives $f_{\rm pl} = 2.2$. Using all the dual frequency measurements in Table 3 with uniform weighting, the geometric emission radii scale with frequency according to $\bar{f}_{\rm geo} = 1.2 \pm 0.1$. Using the emission radii calculated from the delay-radius relation, $\bar{f}_{\rm delay} = 1.3 \pm 0.2$. Since both our experimental estimates of $\bar{f}$ agree and both are small compared with 2.2, it seems that the average scaling of emission radius with frequency is weaker than $\nu^{-2/3}$.

Assuming a power-law relationship between radius and frequency, and taking the average experimental value $\bar{f} = 1.23 \pm 0.15$, the emission radius scales with frequency as $r(\nu) \propto \nu^{-0.2 \pm 0.1}$. It appears that one can find a fairly reasonable theoretical explanation for this scaling. Using equation (5.21) in BGI83, one finds that the radius at which their maser mechanism ceases to amplify radiation scales as $r(\nu) \propto \nu^{-1/3}\gamma^{-1}$. Assuming that γ is constant, the emission radius would scale with frequency according to $r(\nu) \propto \nu^{-1/3}$, which is reasonably consistent with our result. From AS79 one finds that the accelerating potential can vary with radius as $r^{1/2}$. If the Lorentz factor varies as $r^{1/2}$, then the emission radius scales with frequency as $r(\nu) \propto \nu^{-2/9}$, which is totally consistent with our result. We also note that the theoretically obtained emission radii of BGI83 are very similar to the emission radii obtained by us.

6. PROPAGATION EFFECTS

Any realistic treatment of pulsar emission must address the possibility of propagation effects. If the relativistic flow model is correct, then propagation effects cannot significantly alter the radiation after emission. In this section we consider the effects of refraction, mode coupling, and nonlinearity on pulsar radio emission. The calculations will be done in an order-of-magnitude sense; they are not meant to be complete. Before examining individual propagation effects, we point out that the simple relationships considered so far are satisfied within an order of magnitude. Therefore it is unlikely that propagation effects change ray paths or polarization angles by more than a radian. Our emission height estimates depend on measuring angles of a few degrees. If propagation effects of sufficient strength to alter the results of our model exist, it appears that a fine tuning of the ambient conditions in the pulsar magnetosphere must exist. We consider the existence of such a fine tuning to be unlikely.

The first propagation effect we consider is refraction. In the limit that the frequency of the emitted radiation ω is small in comparison with the gyrofrequency in the rest frame of the plasma, the dispersion relation for a relativistic plasma has been obtained (MS77; AB86), and the ray trajectories have been studied (BA86). For a monoenergetic plasma, the amount of refraction may be characterized by the ratio $\Lambda = \omega'_p/\omega'$, where ω'_p and ω', are the plasma and wave frequencies in the frame comoving with the plasma. When $\Lambda \ll 1$, refraction is generally small, and vice versa. Let θ be the angle between the wavevector and the magnetic field where $\gamma^{-1} \lesssim \theta \lesssim 1$. For the fast branch of the dispersion relation, both MS77 and BA86 find

$$\Lambda \sim \frac{\omega_p}{\omega\gamma^{3/2}\theta^2} ,$$

where ω and ω_p are the wave and plasma frequencies in our frame, respectively. As an order-of-magnitude estimate of refraction, we will assume that the radiation has its group velocity parallel to the magnetic field for $\Lambda > 1$, and that the radiation propagates as in free space for $\Lambda < 1$ (BA86). The total change in the direction of the group velocity is equivalent to the refraction angle. For small θ, BA86 find that $d\theta/dr \sim \rho^{-1}$, where ρ is the radius of curvature of the field lines. To obtain the total refraction angle, we assume that the group velocity and the wavevector are parallel at emission. If $\Lambda \gtrsim 1$ at emission, the radiation will be refracted along the field lines until $\Lambda \approx 1$. Since the direction of the wavevector changes more slowly than the direction of the group velocity (BA86), the total refraction angle is nearly the angle between the wavevector and the magnetic field when $\Lambda = 1$;

$$\delta\theta_r \sim \left(\frac{\omega_p^2}{\gamma^3\omega^2}\right)^{1/4} . \qquad (30)$$

For $\Lambda \lesssim 1$ at emission the refraction angle may be estimated using Snell's law. Assuming that the cyclotron frequency is much larger than the wave frequency, the extraordinary mode has an index of refraction $n = 1$. The index of refraction for the ordinary mode differs from unity by an amount (MS77)

$$\Delta n = \frac{2\omega_p^2\theta^2}{\omega^2\gamma^3(\theta^2 + \gamma^{-2})^2} . \qquad (31)$$

The peak value of Δn is for $\theta \sim \gamma^{-1}$, $\Delta n_{\max} \sim \omega_p^2\omega^{-2}\gamma^{-1}$. To estimate the refraction angle crudely, we model the system as a planar interface with $\theta = \gamma^{-1}$ and $n = 1 + \Delta n_{\max}$ on the incident side, and $n = 1$, $\theta = \gamma^{-1} + \delta\theta_r$ in the outgoing side. Snell's law gives $\delta\theta_r \sim \Lambda^2\gamma^{-3}$. As we will find below, the refraction angles predicted by this second estimate will be totally negligible if other propagation effects are no more than marginally important.

Another important issue for propagation effects is the phenomenon of mode coupling and, conversely, independent mode propagation. The central issue involves the rate at which the plasma parameters, and therefore the characteristics of the local normal modes, vary along the path followed by the radiation. If the plasma parameters vary slowly enough, and Δn is large enough, the radiation for each mode will propagate independently and "adiabatically walk" (CR79; S84a,b; B86). While normal-mode propagation is in effect, the polarization angle will twist. The criterion for independent mode propagation depends mainly on the rate at which the polarization of the modes varies along the ray path (Budden 1952; Cohen 1959; Melrose 1979; CR79; Stinebring 1982; B86). This is due to the fact that the coupling between the modes involves a transfer of energy. Currents generated by one of the modes must excite the other mode, for energy transfer to take place.

There are two parameter regimes in which the twist in polarization angle ψ may be calculated easily. In the "adiabatic walking" regime the radiation propagates independently in each of the local normal modes. In the second case the local normal modes change so quickly that the position angle twist rate is constrained by the difference in wavenumber between the normal modes.

$$\frac{d\psi}{dr} \approx \frac{\Delta k}{2} . \qquad (32)$$

In equation (32) Δk is the difference in wavenumber for the two normal modes. For estimation purposes we will assume that the rate at which the polarization angle twists is given by equation (32). In general this will be an upper limit to the actual rate. The total change in position angle will be given by

$$\delta\psi_t \sim \int_{r_e}^{\infty} \frac{\Delta k}{2}\, dr .$$

The estimate the wavenumber difference, we assume that the radiation frequency is negligible compared to the cyclotron frequency, so $\Delta k = \Delta n\omega$, with Δn given by equation (31). For the parameter regimes we will be interested in, the integrand will be small for $\theta \gtrsim (\Omega r_e)^{1/2}$, so we may make the substitution $dr = \rho_c\, d\theta$, where $\rho_c \sim (r_e R_{\rm lc})^{1/2}$ is the radius of curvature of the field lines. We take $\theta = 0$ at emission, giving

$$\delta\psi_t \sim \frac{\omega_p^2\sqrt{r_e R_{\rm lc}}}{\omega\gamma^2} .$$

For unperturbed propagation the RVM predicts that the total position angle change across the pulse is ~ 1, while the width of the pulse is $\sim(\Omega r_e)^{1/2}$. The shift in the centroid of the position angle curve is approximated by $\delta\phi_t \sim (d\psi/d\phi)^{-1}\delta\psi_t \sim (\Omega r_e)^{1/2}\,\delta\psi_t$. For a shift in the pulse center $\delta\phi_t \lesssim \Omega r_e$,

$$\frac{\omega_p^2}{\gamma^2} \lesssim \omega\Omega . \qquad (33)$$

To get a ballpark estimate of the Lorentz factors implied by equations (30) and (33), we assume that the plasma and wave frequencies are equal in the rest frame of the plasma at emission, $\gamma\omega_p^2 = \omega^2$ at $r = r_e$ (CR79). The refraction angle will be approximately γ^{-1} or less, and for the delay-radius relation to remain intact we need

$$\gamma \gtrsim 500 P_s r_7^{-1} . \qquad (34)$$

Using equation (33), the Lorentz factor is constrained to be

$$\gamma \gtrsim 1000 P_s^{1/3} \nu_9^{1/3} . \qquad (35)$$

It is easy to see that when equation (35) is satisfied, adiabatic walking would not alter the delay-radius relation derived in § 2, since the distance over which adiabatic walking effects are important will be equal to the length scale for the decay of Δn, which is always $\lesssim r_e$.

Since low-energy particles interact more strongly with the radiation field than high-energy particles, the inequalities must hold for the lower bound on the Lorentz factor distribution function. For electrons and positrons that undergo the full polar cap potential drop, expected Lorentz factors are $\sim 10^7$ (see, e.g., RS75), which is four orders of magnitude larger than the lower bound obtained by us. It does not seem unreasonable to suppose that most of the plasma particles have energies in excess of 10^{-4} of the maximum particle energy, and, as a result, we find that propagation effects may be unimportant within the context of the relativistic flow model.

It is possible that linearized plasma theory and the accompanying dispersion relations are inadequate for radiative transfer calculations in pulsar magnetospheres. We estimate the importance of nonlinear effects by considering the accuracy of linear theory. For nonrelativistic systems the parameter $\Delta = eE(m\omega)^{-1}$ is an indicator of the strength of nonlinear plasma effects (see, e.g., Davidson 1972). When $\Delta \ll 1$, nonlinear effects are small, and vice versa. For application to the pulsar problem we assume a monoenergetic unperturbed plasma with Lorentz factor γ, and calculate Δ in the rest frame of the plasma. Particle motion orthogonal to the magnetic field is suppressed, so only the component of the electric field that is parallel to the magnetic field gives rise to substantial currents. We assume a nearly transverse electromagnetic wave propagating at an angle θ with respect to the magnetic field and take $\gamma^{-1} \lesssim \theta \lesssim 1$. In the rest frame of the plasma the frequency of the wave is $\omega' \approx \gamma\theta^2\omega/2$. The component of the radiation electric field parallel to the magnetic field is $E_{\parallel} \sim E\theta$. Given these results, the value of the nonlinearity parameter in the comoving frame is $\Delta = eE_{\parallel}(m\omega')^{-1} \approx eE(m\omega\gamma\theta)^{-1}$.

We estimate the radiation electric field by assuming two circular beams of full width 3ω and a total radio luminosity $10^{28}L_{28}$ ergs s^{-1}. Substituting fiducial parameters gives $\Delta \approx 0.5L_{28}^{1/2}(\gamma_3 r_7 \nu_8 \theta_2 w_5)^{-1}$, where $w = 5°w_5$ and $\theta = 2°\theta_2$. The value of the nonlinearity parameter depends quite strongly on several parameters, but it is clear that nonlinear effects can be important.

Beskin, Gurevich, & Istomin (1988) have proposed a nonlinear plasma theory which incorporates a curved magnetic field. It is found that two quasi-transverse radiation modes exist, and both are coupled to the plasma. For a substantial range of magnetospheric parameters the coupling to the plasma appears strong enough to account for the observed orthogonal moding in pulsar radio data. Since both radiation modes couple to the plasma, they must, to some extent, couple to each other. A quantitative analysis of propagation effects in the nonlinear limit is beyond the scope of this paper, but we point out that the nonlinearity should cause propagation effects to be less important than the predictions of linear theory, since the nonlinear theory incorporates additional limitations on the response of the plasma.

7. CONCLUSIONS

The fundamental property of the relativistic flow model is the prediction that the polarization angle curve should lag the intensity profile. Of the 23 pulsars we analyzed, only two are not in accord with the prediction.

Emission radii predicted using the delay-radius relation are of the same order as emission radii obtained in other, independent ways. The estimated radii for radio emission range from 60 to 900 km, with some weak evidence that emission radius increases with frequency. It also appears that core emission may originate at a lower altitude than cone emission. No significant dependence of emission radius on period or period derivative was discovered. Given the uncertainties, the results of the model are consistent with the predictions of a radius–to–pulse-width mapping wherein the radio emission fills the region $\delta^2 \leq \Omega r$, at the emission radius. The agreement between the emission radii obtained via the two methods supports the long-standing assumption that the region of plasma outflow is determined by $\delta^2 \leq \Omega r$ at all radii.

In addition to emission radius estimates, geometrical constraints on pulsar beaming were obtained for several objects. With a confidence of 1 standard deviation, seven objects have emission on field lines that bend away from the spin axis. With the same certainty, only two have emission on field lines that bend toward the spin axis. The observation poses a serious problem for some current magnetospheric models (A83; J86). Additionally, our data are consistent with the spin and magnetic axis being at random angles.

While magnetospheric propagation effects and nondipolar magnetic fields may pertain to radio pulsar magnetospheres, we find it remarkable that the RVM appears to fit pulsar data so well. We also find it remarkable that the first-order relativistic corrections we have considered yield emission radii that are also reasonable. A possible conclusion is that, by combining the RVM with first-order relativistic effects and adding the complicating occurrence of orthogonal polarization modes, the salient features of pulsar polarization are fully accounted for.

We thank Don Backer, Roger Foster, and Joel Weisberg for assisting in the acquisition of the data, which were obtained as part of a long-term timing a polarization monitoring program currently underway at Arecibo. Additionally, we thank Joel Weisberg for calibrating much of the polarization data and Tony Phillips for enlightening conversations. This research was supported by the National Astronomy and Ionosphere Center at Cornell, which operates Arecibo Observatory under contract to the NSF. This work was also supported by the NSF through grants AST 85-20530, AST 87-14475, and AST 89-13112, and by NASA grant NAGW-666 to Cornell University.

REFERENCES

Arons, J. 1983, ApJ, 266, 215 (A83)
Arons, J., & Barnard, J. J. 1986, ApJ, 302, 120 (AB86)
Arons, J., & Scharlemann, E. T. 1979, ApJ, 231, 854 (AS79)
Backer, D. C. 1973, ApJ, 182, 245
Backer, D. C., & Rankin, J. M. 1980, ApJS, 42, 143 (BR80)
Backer, D. C., Rankin, J. M., & Campbell, D. B. 1975, ApJ, 197, 481 (BRC75)
Bailes, M. 1988, A&A, 202, 109
Barnard, J. J. 1986, ApJ, 303, 280 (B86)
Barnard, J. J., & Arons, J. 1986, ApJ, 302, 138 (BA86)
Beskin, V. S., Gurevich, A. V., & Istomin, Ya. N. 1983, Soviet Phys.—JETP, 58, 235 (BGI83)
———. 1986, Soviet Phys. Uspekhi, 29, 946 (BGI86)
Beskin, V. S., Gurevich, A. V., & Istomin, Ya. N. 1988, Soviet Astr. Letters, 14 (No. 2), 93
Biggs, J. D. 1990, MNRAS, 245, 514
Budden, K. G. 1952, Proc. Roy. Soc. London, A, 215, 215
Buschauer, R., & Benford, G. 1976, MNRAS, 177, 109
———. 1980, MNRAS, 190, 945
Chen, K., & Shaham, J. 1989, ApJ, 339, 279
Cheng, K. S., Ho, L., & Ruderman, M. 1986, ApJ, 300, 500
Cheng, A. F., & Ruderman, M. A. 1979, ApJ, 229, 348 (CR79)
Cohen, M. H. 1959, ApJ, 130, 221
Cordes, J. M. 1978, ApJ, 222, 1006
Cordes, J. M., & Hankins, T. H. 1977, ApJ, 218, 484 (CH77)

Cordes, J. M., Rankin, J. M., & Backer, D. C. 1978, ApJ, 223, 961 (CRB78)
Cordes, J. M., & Stinebring, D. R. 1984, ApJ, 277, L53
Cordes, J. M., Wasserman, I., & Blaskiewicz, M. 1990, ApJ, 349, 546
Cordes, J. M., Weisberg, J. M., & Boriakoff, V. 1983, ApJ, 268, 370
Cordes, J. M., Wolszczan, A., Dewey, R. J., Blaskiewicz, M., & Stinebring, D. R. 1990, ApJ, 349, 245
Davidson, D. C. 1972, Methods in Non-linear Plasma Theory (New York and London: Academic).
Ferguson, D. C. 1973, ApJ, 183, 977
———. 1976, ApJ, 205, 247
Ferguson, D. C., & Boriakoff, V. 1980, ApJ, 239, 310
Goldreich, P., & Julian, W. H. 1969, ApJ, 157, 869 (GJ69)
Goldreich, P., & Keeley, D. A. 1971, ApJ, 170, 463
Hankins, T. H., & Cordes, J. M. 1981, ApJ, 249, 241
Jackson, J. D. 1975, Classical Electrodynamics (New York: Wiley)
Jenkins, G. M., & Watts, D. J. 1968, Spectral Analysis and Its Applications (Oakland: Holden-Day)
Jones, P. B. 1986, MNRAS, 222, 577 (J86)
Krishnamohan, S., & Downs, G. S. 1983, ApJ, 265, 372
Lindgren, B. W. 1962, Statistical Theory (New York: Macmillan)
Lyne, A. G., & Manchester, R. N. 1988, MNRAS, 234, 477 (LM88)
Manchester, R. N., & Lyne, A. G. 1977, MNRAS, 181, 761
Manchester, R. N., Taylor, J. H., & Huguenin, G. R. 1975, ApJ, 196, 83 (MTH75)
Matese, J. J., & Whitmire, D. P. 1980, ApJ, 235, 587
Melrose, D. B. 1978, ApJ, 225, 557
———. 1979, Australian J. Phys., 32, 61
Melrose, D. B., & Stoneham, R. J., 1977, Proc. Astr. Soc. Australia, 3, 120 (MS77)
Mestel, L. 1971, Nature Phys. Sci., 233, 149
———. 1973, Ap&SS, 24, 289
Michel, F. C. 1982, Rev. Mod. Phys., 54, 1 (M82)
Narayan, R., & Vivekanand, M. 1982, A&A, 113, L3 (NV82)
———. 1983, A&A, 122, 45 (NV83)
Phillips, J. A. 1990, ApJ, 361, L57
Phillips, J. A., & Wolszczan, A. 1990, Low-Frequency Astrophysics from Space (Lecture Notes in Physics; New York: Springer Verlag)
Radhakrishnan, V., & Cooke, D. J. 1969, Ap. Letters, 3, 225
Rankin, J. M. 1983, ApJ, 274, 331 (R83)
———. 1986, ApJ, 301, 901 (R86)
———. 1990, ApJ, 352, 247 (R90)
Rankin, J. M., Wolszczan, A., & Stinebring, D. R. 1988, ApJ, 324, 1048
Ruderman, M. A., & Sutherland, P. G. 1975, ApJ, 196, 51 (RS75)
Schönhardt, R. E., & Sieber, W. 1973, Ap. Letters, 14, 61
Shitov, Y. P. 1985, Soviet Astr., 29 (No. 1), 33 (S85)
Smirnova, T., & Shishov, U. 1989, Soviet Astr. 15, 191
Stinebring, D. R. 1982, Ph.D. thesis, Cornell University
Stinebring, D. R., Cordes, J. M., Rankin, J. M., Weisberg, J. M., & Boriakoff, V. 1984a, ApJS, 55, 274 (S84a)
Stinebring, D. R., Cordes, J. M., Weisberg, J. M., Rankin, J. M., & Boriakoff, V. 1984b, ApJS, 55, 279 (S84b)
Sturrock, P. A. 1971, ApJ, 164, 529 (S71)
Weisberg, J. M., Romani, R. W., & Taylor, J. H. 1989, ApJ, 347, 1030
Wolszczan, A., & Cordes, J. M. 1987, ApJ, 320, L35